Article:
Askari, H., Shariatinia, Z., Tafreshi, S.S. et al. (1 more author) (2024) Spiro[fluorene-9,9'-xanthene] core comprising green imidazole-sulfonylurea moieties devised as excellent hole transport materials for perovskite solar cells. Inorganic Chemistry Communications, 169. 113103. ISSN: 1387-7003

https://doi.org/10.1016/j.inoche.2024.113103

Spiro[fluorene-9,9'-xanthene] core comprising green imidazole-sulfonylurea moieties devised as excellent hole transport materials for perovskite solar cells

Hossein Askari,[a] Zahra Shariatinia,[1*,a] Saeedeh Sarabadani Tafreshi,[a,b] Nora H. de Leeuw[b,c]

[a]Department of Chemistry, Amirkabir University of Technology (Tehran Polytechnic),

P.O.Box:15875-4413, Tehran, Iran.

[b]School of Chemistry, University of Leeds, LS2 9JT Leeds, UK

[c]Department of Earth Sciences, Utrecht University, 3584 CB Utrecht, The Netherlands

[1]*Corresponding author.
E-mail: shariati@aut.ac.ir

Abstract

Fifteen green and benign imidazole-sulfonylurea derivatives of Spiro[fluorene-9,9'-xanthene] (SFX) were devised as hole transporting materials (HTMs) for perovskite solar cells (PSCs) by density functional theory (DFT) method to evaluate their capability of hole extraction from perovskite and transportation within photovoltaic devices. It was indicated that in all HTMs, the highest occupied molecular orbital (HOMO) levels were situated between energy levels of $CsPbCl_3$ perovskite's valence band and Ag electrode's potential, verifying such SFX-based materials could efficiently extract and transfer holes from $CsPbCl_3$ towards Ag contact. The absorption spectra showed that the absorption peaks of all molecules advantageously occurred in the UV (ultraviolet) region (a similar behavior like Spiro-OMeTAD), which certified they did not compete with the $CsPbCl_3$ perovskite in absorbing solar visible light. Also, smaller hole reorganization energy values were obtained for all samples than their corresponding electron reorganization energy values. Notably, for all SFX-based materials, hole mobilities (μ_h) changed from 0.469 to 13.748 $cm^2V^{-1}s^{-1}$, which were very much larger (by about 10^3-10^5 times) than μ_h values of Spiro-OMeTAD. Moreover, all SFX-based HTMs revealed almost equal fill factors (FFs) of 0.929 and very comparable high open-circuit voltage (V_{OC}) values (1.858-1.898 V). Such surprising results substantiated that these green and biocompatible imidazole-sulfonylurea derivatives of SFX could be applied as excellent HTM alternatives for the famous and commercial Spiro-OMeTAD to fabricate high-performance PSC photovoltaics.

Keywords: SFX; Perovskite solar cells; Imidazole-sulfonylurea substituents; DFT computations; UV-Vis absorption and photoluminescence spectra

1. Introduction

In recent years, the rapid increase in energy demand has enhanced efforts by researchers to find energy resources as alternatives to fossil fuels and other conventional sources [1]. Solar cells have been developed as powerful candidates to compete with prominent energy generation technologies in electricity generation from sunlight as an ecological, renewable, and green energy resource [2, 3]. Huge solar energy received by earth is converted to electricity using efficient photovoltaic devices to provide required global energy. For this purpose, great efforts have been performed to achieve cheap and reliable solar cells [4]. Therefore, the photovoltaic process is known as a potential mechanism to generate renewable energy that has received lots of attention.

PSCs are a novel type of photovoltaic systems. By rapid development since its launch in 2009, the state-of-the-art PSC afforded a validated PCE of up to 25.2%, like traditional silicon solar cells [5]. Because perovskite materials display exceptional features, PSCs exhibit excellent photovoltaic performances and this is due to the progressive development/optimization of materials, which are composed of specific structures and functional groups [6].

PSCs are fabricated using organic, organic-inorganic, and inorganic halide perovskites because these materials exhibit high performances [7, 8]. The first inorganic perovskite (cesium lead halide) was used by Loredana Protesescu et al. and since then lots of researches have been done on application of these efficient materials ($CsPbX_3$; X = I, Cl, Br, and their combinations) in PSCs. Inorganic perovskites reveal suitable crystallinity, great photoluminescence quantum yield (by 90%), low emission linewidth, and small size distribution, which make them become a research hotspot [9]. This is related to exceptional optical characteristics, high

photoluminescence intensity, defect tolerance, band gap tunability, and easy synthesis methods of such materials [10, 11].

To commercialize PSCs, it is important to replace the Au electrode with its alternatives to reduce the unit cost [12]. From the early stage, Ag is usually utilized as cathode of PSCs because it displays favorable stability and conductivity [13]. Some Ag properties makes it an advantageous electrode including (1) price: it is more inexpensive compared to Au, which makes it more cost-effective in scale up of affordable PSCs as it reduces the overall manufacturing cost [14]. (2) Optical characteristics: it shows outstanding absorption and scattering of light, which are very imperative in high-performance PSC devices. (3) Stability: Ag has a high chemical stability without any easily reaction with electrolyte and perovskite existing in the PSC structure, which results in longstanding device stability under light exposure in most practical applications, but its stability can be influenced by environmental factors and the presence of certain reactive species. Also, prolonged exposure to intense light and environmental factors could potentially affect the device's stability, though this is more related to the overall device design and encapsulation rather than the intrinsic properties of silver. In case of $MAPbI_3$ perovskite, Au diffusion into $MAPbI_3$ can cause effective non-radiative recombination and device degradation. (4) Reflection: Ag unveils suitable reflection property that boosts trapping/absorption of photons in device and improves efficiency [15].

In PSCs, solid hole transport materials were emerged as a crucial innovation to replace liquid electrolyte materials [16, 17]. An ideal HTM should have advantages including upper HOMO energy than perovskite’s valence band (VB) level, minimum visible and near-infrared absorption, low price, benign nature, high hole mobility, and superb thermal and photo-chemical

stability [18]. HTMs unravel many effects within PSC devices because they act as energy and physical barriers between the metal/carbon electrode and perovskite to prevent backward electron transportation. Furthermore, HTMs improve hole transfer rate and influence V_{OC} values [19].

Spiro-OMeTAD is the most commonly used and popular HTM with high efficiency for both PSCs and solid-state dye-sensitized solar cell (DSSC) [20]. Nevertheless, in pure form, it indicated weak conductivity ($\sim 10^{-5}$ Scm^{-1}) and hole mobility ($\sim 10^{-4}$ $cm^2V^{-1}s^{-1}$), which resulted in power conversion efficiency (PCE) of 0.7% in solid-state DSSC [21]. When its blend with two additives (including lithium 4-tertbutylpyridine and bis(trifluoromethyl sulphonyl) imide) was used in DSSC, the PCE was boosted to 2.6% [22, 23]. Also, other p-dopants were added as additives to increase its hole mobility such as FK102 Co(III) complex, which showed a PCE of 7.2% [20].

SFX is another alternative to spirobifluorene core existing in the Spiro-OMeTAD structure [24]. SFX core is an attractive green and ecological semiconductor for application in PSC photovoltaics, which shows a facile one-step synthesis process [25]. Nowadays, researchers seek benign materials and synthesis methods conforming to green chemistry principles. Therefore, natural materials can be chosen to develop semiconductor molecules for optoelectronic devices [26]. Ideal green semiconductors should have basic characteristics including application of renewable/biomass derived compounds, ecological water soluble and film forming materials, atom economic synthesis methods, benign and biodegradable materials, and consume a lower production energy [27]. SFX is composed of xanthene and fluorene fragments that belong to a class of aromatic compounds applied in green eco-friendly organic semiconductors [28].

DFT computations have frequently been used to predict the structural and electronic characteristics of various kinds of molecules. The reason behind the popularity of DFT computational methods can be ascribed to the fact that the calculated data most often exhibit very good agreement with the experimental results. For example, synthesis, molecular structures, and DFT studies were done on (*Z*)-2-((*E*)-4-nitrobenzylidene)hydrazone)-1,2-diphenylethan-1-one [29], benzildihydrazone and benzil monohydrazone based Schiff bases [30, 31], which proved high capability of DFT approaches to correctly measure and predict the molecular properties.

Here, several eco-friendly HTMs were devised for PSCs based on SFX core so that the natural imidazole-sulfonylurea moiety was bound onto *para*-positions of two phenyl rings to obtain functionalized SFX (called f-SFX) and then 15 different substituents were attached to the imidazole-sulfonylurea moiety including $CH_2C(O)OH$ (1), H (2), SH (3), OH (4), OCH_3 (5), $CH_2C(O)OCH_3$ (6), CH_3 (7), SCH_3 (8), $CH_2C(O)SCH_3$ (9), $CH_2C(O)SH$ (10), OCF_3 (11), $CH_2C(O)OCF_3$ (12), CF_3 (13), SCF_3 (14), $CH_2C(O)SCF_3$ (15) (Fig. 1). Using DFT calculations, structures of these materials were optimized to determine ideal samples of superlative hole transfer capacities. It should be noted that the PSCs had an architecture composed of SnO_2 as ETM (electron transfer material), $CsPbCl_3$, and Ag electrode.

In fact, the novelty of this work is application of imidazole and sulfonylurea as benign and sustainable materials that were linked together to form a new imidazole-sulfonylurea moiety, which was attached to the two phenyl rings of SFX core. Notably, both of the imidazole and sulfonylurea groups are familiar drugs used in medicinal chemistry to treat varied illnesses. Therefore, the designed HTMs can be regarded as green semiconductors, which do not have any

adverse effects to the living organisms and environment and can be proposed for practical fabrication and usage of PSC devices.

2. Computation methods

DFT calculations and optimization of HTM structures were done by Gaussian 03 software [32]. HTM derivatives were based on the SFX core composed of fifteen substituents attached to the imidazole-sulfonylurea moiety. In this study, B3LYP/6-31G(d,p) is employed to optimize molecules within both gas phase and dichloromethane solvent. Furthermore, the dipole moments, frontier molecular orbitals (FMOs), hole/electron mobility, and reorganization energies were attained by means of B3LYP/6-31G(d,p) approach. Using frequency computations, the infrared (IR) spectra were obtained. Also, time dependent-DFT (TD-DFT) calculations were performed to acquire the UV-Vis absorption and photoluminescence (PL) emission spectra.

Light harvesting efficiency (LHE) was calculated by Eq. (1), where f_{max}^{abs} displays oscillator strength of absorption.

$$LHE = 1 - 10^{-f_{max}^{abs}} \quad (1)$$

Exciton binding energy (E_b) defines the energy difference between neutral exciton and two free charge carriers. It is estimated using Eq. (2), where E_g indicates electronic band gap that is substituted by energy gap (Δ_{H-L}), whereas E_x exhibits optical gap that is commonly replaced by first singlet emission energy (E_1).

$$E_b = \Delta_{H-L} - E_1 = E_g - E_x \quad (2)$$

Hole transfer capacities of HTMs are calculated theoretically based on Marcus principle and hopping theory [24]. The hole reorganization energy (λ_h) is sum of two parameters ($\lambda_1+\lambda_2$) that are explained by Eqs (3)-(5).

$$\lambda_1=E(M^+) - E(M^+)^* \quad (3)$$

$$\lambda_2=E(M^+) - E(M) \quad (4)$$

$$\lambda_h =\lambda_1+\lambda_2 \quad (5)$$

$E(M^+)$ exhibits energy of minimized cation, $E(M^+)^*$ shows single point energy of neutral molecule from minimized cation, and E(M) demonstrates energy of minimized neutral molecule [33]. Likewise, electron reorganization energy (λ_e) equals to $\lambda_3+\lambda_4$ and can be defined by Eqs. (6)-(8), where $E(M^-)^*$ is single point energy of neutral structure from minimized anion while $E(M^-)$ reveals energy of minimized anion.

$$\lambda_3= E(M^-) – E(M^-)^* \quad (6)$$

$$\lambda_4= E(M^-) – E(M) \quad (7)$$

$$\lambda_e = \lambda_3 + \lambda_4 \quad (8)$$

The adiabatic ionization potential (AIP) and adiabatic electron affinity (AEA) are obtained using Eqs. (9)-(10). Absolute hardness (η) is achieved by Eq. (11).

$$AIP= E (M^+) – E (M) \quad (9)$$

$$AEA= E(M) – E (M^-) \quad (10)$$

$$\eta = (AIP - AEA)/2 \quad (11)$$

To compute hole mobility values of SFX-based HTM samples, their crystal structures and unit cells should be obtained. For this purpose, Materials Studio software [34] was used and geometries of fifteen HTMs were first optimized by Dmol3 module using generalized gradient

correlation approximation (GGA) with Perdew-Burke-Ernzerhof (PBE) functional and DNP (digital dual polarization) basis set [35]. Total charge of each minimized molecule was set to 0 because total electrostatic surface potential (ESP) charge was not exactly 0.0 due to truncation errors when using Dmol3 module. After that, Polymorph module was used with Dreiding force field to obtain crystal structure and unit cell for each sample. Dreiding force field reproduces experimental data very well. For an excellent precision, 10 imperative space groups were simulated, i.e., C2/c, Cc, $P2_1$, $P2_1/c$, $P2_12_12_1$, P-1, $Pna2_1$, C2, Pbcn, and Pbca.

3. Results and discussions

It is known that the DFT methods are very popular that can be used to estimate a diversity of molecular characteristics. In fact, DFT is an economical methodology, which is employed to accurately calculate optical and electronic features of small and rather big molecules [36, 37]. In fact, precise estimation of adiabatic ionization potential, adiabatic electron affinity, and frontier molecular orbital energy is very substantial because these parameters are applied to determine different characteristics of materials such as exciton binding energy and electron/hole injection pathway, which greatly affect PSC performance [38]. Besides, using exact HOMO and LUMO energy levels, one can select the best HTMs for PSCs. Therefore, DFT is used as a theoretical, very common, and reliable method to precisely predict properties of HTMs. Sheerin Naqvi et al. performed DFT calculations on three thiophene-based small molecules at B3LYP level of theory, to estimate their optical and electrical properties. They found that the calculated results agreed well with the experimental values, approving the accuracy of the DFT calculations [39]. Zhan et al. found that DFT computations using B3LYP method and 6-311G(d) basis set could provide

calculated values close to experimental data for hardness, AEA, AIP, electronegativity, and electronic excitation energy [40]. Zhaoning Li et al. calculated absorption spectrum for SFX-diol by MPW1PW91, CAM B3LYP, ωB97XD, and B3LYP methodologies using 6-31G(d,p) basis set and discovered that B3LYP/6-31G(d,p) provided a spectrum that was most similar to its experimental spectrum [41]. As a result, in this work, B3LYP/6-31G(d,p) is used to investigate diverse properties of the designed HTMs in both gas phase and dichloromethane solvent.

The burgeoning field of organic electronics offers immense potential for creating flexible, lightweight, and low-cost devices. However, the environmental impact of traditional organic semiconductors has raised significant concerns. This has spurred a growing demand for eco-friendly alternatives and researchers have endeavored to develop HTMs with the desired properties. Inspired by this ecological strategy, herein, imidazole and sulfonylurea were chosen as non-toxic and eco-friendly materials and linked together to obtain a novel moiety named imidazole-sulfonylurea, which was attached to the two aromatic phenyl rings of SFX core. Then, 15 various biologically important substituents were bound onto the imidazole-sulfonylurea unit. It is noteworthy that both of the imidazole and sulfonylurea groups are well-known drugs used in pharmaceutical chemistry for the treatment of diverse diseases [42, 43]. Here, the materials design is based on the non-toxicity, biocompatibility, and accessibility of the organic groups that are chosen to attach onto the SFX core. To assess various properties of the devised HTMs, calculations of dipole moments, FMOs, hole/electron mobility, and reorganization energies were performed. Last but not least, it can be said that the HTMs designed in this study will have a great potential to be used in practical PSC fabrication in the future.

DFT calculations were carried out to examine structural, electronic, optical, and hole- and electron-transfer characteristics of diverse f-SFX-based HTM compounds for PSCs. For this purpose, a general procedure is followed to explore charge transfer and optoelectronic characteristics of studied molecules. In fact, one can introduce suitable molecules as HTMs considering results achieved from varied analyses and this is a commonly valid method for designing efficient HTMs. An excellent HTM displays several characteristics including: (1) HOMO energy level between VB of perovskite and cathode's Fermi level (e.g. Au and Ag), (2) higher LUMO level than perovskite's conduction band (CB) to prevent backward electron transfer toward cathode, (3) smaller EA and IP, (4) smaller electrophilicity index (ω) and electronegativity (χ), exhibiting its lower electron withdrawing capability, (5) higher chemical hardness (η) and chemical potential (μ), indicating greater stability, (6) larger negative binding energy, (7) higher LHE, (8) smaller E_b, (9) high solubility, (10) lower reorganization energy, bigger hole mobility, greater charge transfer rate/integral, and (11) larger PCE, J_{SC}, V_{OC}, and FF parameters.

3.1. Geometry minimization

A stable geometry has a high influence onto optoelectronic properties of the HTM. Here, DFT method was applied to optimize geometries of 15 HTMs based on SFX core at B3LYP/6-31G(d,p) theoretical level. The structures of these HTMs contained imidazole-sulfonylurea moiety bound onto *para*-carbon atoms of two six-membered rings of SFX core that formed functionalized SFX (called f-SFX), onto which various 15 substituents were attached to the imidazole-sulfonylurea moiety, including $CH_2C(O)OH$ (1), H (2), SH (3), OH (4), OCH_3 (5), $CH_2C(O)OCH_3$ (6), CH_3 (7), SCH_3 (8), $CH_2C(O)SCH_3$ (9), $CH_2C(O)SH$ (10), OCF_3 (11), $CH_2C(O)OCF_3$

(12), CF_3 (13), SCF_3 (14), $CH_2C(O)SCF_3$ (15) (Fig. 1). Notably, HOMO energies matched well with energy levels of materials utilized in PSC devices, i.e. SnO_2 ETM, perovskite $CsPbCl_3$, and Ag electrode. As a result, additional DFT studies were accomplished to explore more features of such HTMs. Fig. 2 displays the most stable structures of devised HTMs.

3.2. Frontier molecular orbital (FMO)

Based on FMO analysis, one can examine electronic and charge transport properties of molecules to select the best HTMs, which can boost the PSC performance. Distribution models calculate HOMO and the lowest unoccupied molecular orbitals (LUMOs), along with their energy levels. FMOs are frequently used to explain charge transfer by semiconductors as highly delocalized FMOs lead to quicker transportation of charges via decreasing reorganization energy of nucleus while boosting electronic interactions of nearby particles.

When discussing hole transportation in a material, it is essential to study movement of positive charge carriers, generally denoted as holes. Hole can be conceptualized as absence of an electron within a specific orbital. HOMO of a molecule is the orbital from which an electron is removed to generate a hole. More HOMO delocalization is beneficial to boost hole transfer integral. Electron density distribution in HOMO influences hole mobility. If HOMO has a greater electron density, it has a more probability of finding an electron in the orbital. This higher electron density in HOMO is usually correlated to more effective hole generation/mobility because there are more existing electrons to produce such mobile positive charges [44].

FMOs describe charge transfer and electron density distribution. Fig. 3 depicts FMOs for all the HTMs based on the SFX core and imidazole-sulfonylurea substituent. Negative and positive

charges are represented in green and red colors, respectively. As Fig. 3 exhibits, LUMO orbitals in all HTMs are primarily spread over central SFX core. Besides, HOMO orbitals of nine compounds (f-SFX-$CH_2C(O)OH$, f-SFX-H, f-SFX-OH, f-SFX-OCH_3, f-SFX-$CH_2C(O)OCH_3$, f-SFX-CH_3, f-SFX-OCF_3, f-SFX-$CH_2C(O)OCF_3$, f-SFX-CF_3) are distributed more broadly than their LUMO orbitals, which may display these studied derivatives have a higher potential as HTMs. On the other hand, six sulfide-containing structures (f-SFX-SH, f-SFX-SCH_3, f-SFX-$CH_2C(O)SCH_3$, f-SFX-$CH_2C(O)SH$, f-SFX-SCF_3, f-SFX-$CH_2C(O)SCF_3$) show slight distributions of HOMO orbitals over the molecules.

Tables S1 and Table 1 demonstrate the HOMO and LUMO energies and band gaps (E_g) in gas phase and dichloromethane solvent for the 15 HTMs comprising green imidazole-sulfonylurea group bound onto *para*-carbon atoms of two six-membered rings of SFX, respectively. Dichloromethane solvent has been selected as it is the most extensively applied solvent in majority of experimental studies [45, 46]. In PSC devices, light absorption by the perovskite produces electrons and holes. The light-excited electrons are injected into conduction band of SnO_2 ETM, transferred through SnO_2, and collected via fluorine-doped tin oxide (FTO) conductive substrate. Moreover, holes in VB of perovskite are transferred towards HTM. Accordingly, the HOMO energy of an efficient HTM must be between the $CsPbCl_3$ perovskite's VB (-6.5 eV) and Ag work function (-4.7 eV). Also, LUMO energy of HTM should be higher compared to perovskite's CB to stop backward electron transfer from perovskite towards HTM, thereby reducing recombination of charges through electron blocking influence. Energy levels of FTO, SnO_2, $CsPbCl_3$ perovskite, f-SFX-based HTMs, as well as Ag electrode are presented in Fig. 4, confirming all 15 samples are satisfactory HTMs for such PSC devices.

Beside the graphical picturing of HOMO and LUMO energy levels, one can investigate electronic features of HTMs through analyzing FMOs energies. Fig. 4 exhibits that HOMO energies of all molecules are located above -5.9 eV, displaying they are higher than VB of perovskite $CsPbCl_3$ (-6.5 eV). This observation approves that holes can be successfully transferred from $CsPbCl_3$ to HTM samples. Perovskite's CB must be lower than LUMO energy of HTM to effectually suppress electron transportation from perovskite to Ag electrode. CB of perovskite (-3.8 eV) is very deeper compared to LUMO energies of devised HTM compounds, verifying effective electron blocking happens. Consequently, all HTMs can satisfactorily suppress electron transfer from perovskite to Ag cathode. The difference between VB of SnO_2 and HOMO level of HTM can be correlated to V_{OC} in PSCs [47]. The deeper HOMO of HTM can result in a higher V_{OC} for the PSC, emphasizing an essential driving force for hole injection from $CsPbCl_3$ toward HTM.

The energy difference between HOMO and LUMO orbitals is called band gap (E_g), which can visually be indicated by the density of states (DOS) spectra. The DOS spectra of the f-SFX-based HTMs are displayed in Fig. S1. It is observed that all HTMs have comparable E_g values of about 4.3-4.4 eV.

3.3. Solubility and dipole moment

Material's solubility is an essential parameter, being defined by solvation free energy (ΔG_{solv}), which is calculated using Eq. (12) [48]. It should be noted that the ΔG values in both gas phase and solution (ΔG_{sol} and ΔG_{gas}) are extracted from the results obtained by frequency calculations at 298 K. Dichloromethane solvent was selected herein and ΔG_{solv} values of all HTMs are given in Table 2. Large negative solvation free energies attained for all samples illustrate that

their solvation occurs spontaneously, indicating their high solubility that is beneficial in practical experiments for deposition of HTMs over the perovskite layer.

$$\Delta G_{solv} = \Delta G_{sol} - \Delta G_{gas} \quad (12)$$

Dipole moment can be used as another key factor to estimate molecular solubility so that solubility within polar solvents is higher if dipole moment is larger. Good solubility and film formation properties are valuable for material deposition through spin-coating and result in optimized packing of layers, shape, and surface interaction with perovskite's film [49, 50]. Better solubility allows using a broader range of HTM concentrations and more solvents, affording optimum optoelectronic features. The dipole moment can be related to ESP because the ESP map indicates distributions of positive and negative charges above molecular structure. Fig. 5 shows ESPs of all f-SFX-based HTMs, which can be used to estimate the molecular polarity visually. The contour maps of f-SFX-based HTMs are presented in Fig. S2. Furthermore, changes of dipole moments of all HTMs in both gas phase and dichloromethane solution are provided in Fig. 6a.

As Table 2 reveals, dipole moments in dichloromethane solution are very larger than their related values in the gas phase. The dipole moments vary in the ranges of 10.97-17.44 Debye and 16.25-27.11 Debye in gas phase and dichloromethane solution, respectively. In addition, f-SFX-CH_3 and f-SFX-$CH_2C(O)SCF_3$ unveil the lowest and the largest dipole moments in CH_2Cl_2 solvent, respectively.

Binding energy ($E_{binding}$) values of samples are estimated using the formula $E_{binding} = E_{HTM} - \Sigma E_{atom}$, where E_{HTM} and E_{atom} present the energies of optimized HTM and atom, respectively. Table 2 exhibits that $E_{binding}$ values of HTMs change in the range of -11120.16 kcal/mol (for f-SFX-H) to

-13134.21 kcal/mol (for f-SFX-$CH_2C(O)OCF_3$). Furthermore, highly negative binding energies of all samples validate their high stability.

3.4. Ionization potential and electron affinity

To elucidate charge transport efficiency, the two important parameters including AIP and AEA are obtained using DFT method to estimate amounts of energies needed to inject hole and electron, respectively. A lower AIP indicates an improved hole transportation property whereas a larger AEA> 3 will result in an enhanced electron transportation feature [28].

AIP has a direct relationship with hole injection by the HTM. Generally, HTM with a lower AIP reveals a more effective hole injection. The f-SFX-based HTMs exhibit almost identical (very close) AIP values of about 6 eV so that the f-SFX-OCF_3 and f-SFX-CF_3 indicate the biggest AIP = 5.988 eV but f-SFX-CH_3 displays the lowest AIP value of $5.900\ \mathrm{eV}$. This result may verify that all samples have nearly comparable capacities for hole transfer so that f-SFX-CH_3 the most easily supports hole transportation.

Appropriate HTMs of PSCs must exhibit small AEA because they accept holes from $CsPbCl_3$ and transport them toward Ag electrode. Therefore, data in in Table 2 reveal that all HTMs with AEA<3 are desirable hole transporting agents. The AEA values vary from $-1.758\ \mathrm{eV}$ (in f-SFX-CH_3) to $-2.713\ \mathrm{eV}$ (in f-SFX-CF_3). Hence, it can be decided that SFX-CH_3 with the smallest AEA is the best HTM, based on the AEA results.

3.5. Infrared (IR) spectra

Fig. 6b depicts IR spectra of devised HTMs attained in CH_2Cl_2 solvent. There are some peaks of varied intensity within IR spectra. Also, the IR spectra are extended within wavenumber region of 400-1900 cm^{-1} and presented as Fig. S3, making it easier to discern peak positions and corresponding vibrational modes. Bands placed close to 3000-3200 and 3600-3800 cm^{-1} indicate stretching modes of C-H, N-H, O-H bonds, respectively. Some bands positioned near 1100 cm^{-1} exhibit stretching vibrations of C-O bonds whereas bands at approximately 1350 and 1550 cm^{-1} exhibit symmetric and asymmetric stretching vibrations of C=C bonds [51]. Bands perceived at around 600-800 cm^{-1} reveal bending vibration of C-H bond. Peaks placed at around 1650 cm^{-1} demonstrate bending vibrations of O-H bonds [52, 53]. Moreover, peaks observed at nearly 1000 and 900 cm^{-1} exhibit stretching of C-N and C-S bonds, respectively [54].

3.6. Molecular descriptors

Molecular descriptor parameters are achieved to inspect stability and reactivity of HTMs and the results are collected in Table 3. To estimate electron donation properties of HTMs, their chemical potential (μ) values are measured. Eq. (13) is used to calculate chemical potentials of molecules. High negative chemical potentials of all HTMs (in the range of -3.745 to -3.854 eV) demonstrate that they are very stable and reactive compounds. Additionally, high μ values of these materials suggest that they can effectively donate electrons. All SFX-based samples display greater negative chemical potentials compared to values reported for X65 (μ=-2.46) [55] and calculated for Spiro-OMeTAD (μ=-2.719 eV, see Table 3) as standard HTMs, validating they are highly stable molecules.

$$\mu = 1/2\ [E_{HOMO} + E_{LUMO}] \qquad (13)$$

Hardness (η) can be directly related to stability and obtained using Eq. (14). It shows molecular resistance against changing its quantity of electrons, which affects PSC stability because HTM has a critical influence on device stability. An ideal HTM is a stable material, which indicates a big η. Table 3 records the calculated η values for HTM structures. Evidently, all η amounts are very similar that alter in a limited range of 2.142-2.213 eV. This result approves that all investigated HTM molecules have almost similar stabilities that are higher than η= 1.71 eV calculated for Spiro-OMeTAD (see Table 3) as a famous and commercially used HTM for PSC devices.

$$\eta = 1/2\ [E_{LUMO} - E_{HOMO}] \qquad (14)$$

$$S = 1/\eta \qquad (15)$$

Chemical softness (S) is obtained for a material using Eq. (15). A higher S value suggests that the molecule donates electrons effectively and has a high reactivity with its neighboring molecules. It is seen that the S values of all HTMs are very similar and change from 0.452 eV (in f-SFX-CH_3) to 0.467 eV (in f-SFX-OCF_3). Such data confirm that these HTMs have comparable reactivities that are close to S=0.561 eV for the well-known Spiro-OMeTAD.

Electrophilicity index (ω) and electronegativity (χ) are calculated by Eqs. (16) and (17), respectively. These parameters are generally related to each other and demonstrate electron-withdrawing feature of a molecule.

$$\omega = 1/2\ [\chi^2/\eta] \qquad (16)$$

$$\chi = -\ 1/2\ [E_{HOMO} + E_{LUMO}] \qquad (17)$$

The ω and χ parameters change within ranges of 3.170-3.467 eV and 3.745-3.854 eV, respectively, verifying the devised f-SFX-based HTMs have comparable electron attracting

capabilities. f-SFX-CH_3 has the lowest χ and ω values, which may confirm this is the most favorable HTM.

As another crucial parameter, maximum charge transfer (ΔN_{max}) values of f-SFX-based HTMs are estimated by Eq. (18). As Table 3 reveals, charge transfer capacities of f-SFX-based HTMs are superior to ΔN_{max}=1.526 measured for Spiro-OMeTAD. Besides, the charge transfer values vary from 1.693 (in f-SFX-CH_3) to 1.799 (in f-SFX-OCF_3). Consequently, these samples can be excellent HTMs for photovoltaic PSCs.

$$\Delta N_{max} = -\mu/\eta \qquad (18)$$

3.7. Optical properties

Light harvesting efficiency (LHE) unveils material's ability for absorption of solar photons [56, 57]. If f_{abs}^{max} is greater, the light absorption capacity is enhanced. Grätzel et al. realized that HTMs of large LHEs are able to boost generation of photocurrent in PSCs [58]. Table 4 presents maximum wavelengths of absorbance (λ_{abs}^{max}) and emission (λ_{em}^{max}), main transitions in absorption spectra (transition probability), LHEs, oscillator strength (f_{abs}), and Stokes shift (λ_{ss}). LHE values achieved within the range of 0.351-0.622 for the f-SFX-based HTMs approve their relatively favorable light absorption abilities. The largest LHEs are measured for f-SFX-OCF_3 (0.622) and f-SFX-CF_3 (0.620) whereas f-SFX-$CH_2C(O)SCF_3$ unveils the smallest LHE= 0.351.

Fig. 7a provides UV-Vis absorption spectra of f-SFX-based substances. All samples illuminate one broad peak along with a shoulder in the wavelength region of 302.32-309.58 nm, indicating all molecules have absorption peaks in the UV spectral region. This behavior is like Spiro-OMeTAD that shows an absorption peak at λ_{abs}^{max} <400 nm, signifying it is not a rival to

perovskite material for visible light absorption. Furthermore, the highest peak intensities can be detected for f-SFX-$CH_2C(O)SCH_3$ and f-SFX-SCH_3 while the lowest peak intensities belong to f-SFX-CF_3 and f-SFX-OH.

It is obvious from Table 4 that the main transition in absorption spectra of all samples is attributed to the H-1→L+1, except for the f-SFX-CH_3 indicating H→L+1 as the main electronic transition. Also, the transition probabilities for the main transitions related to the λ^{max}_{abs} peaks vary from 31.87% (f-SFX-$CH_2C(O)OH$) to 55.36% (f-SFX-OCF_3).

Fig. 7b presents PL emission spectra for the devised HTMs within CH_2Cl_2 solution. It is obvious that the $\lambda_{em}{}^{max}$ values of all HTMs appear at higher wavelengths than their related $\lambda_{abs}{}^{max}$ values in the absorption spectra. This is reasonable as there are always thermal and non-thermal or radiative energy losses during emissions. The $\lambda_{em}{}^{max}$ values of SFX-based materials vary from 317.13 nm (in f-SFX-H) to 325.50 nm (in f-SFX-$CH_2C(O)SCF_3$).

Stokes shift reveals difference in maximum wavelengths of emission PL and UV-Vis absorption spectra. In fact, differences of molecular geometries at ground and excited states are correlated to Stokes shift that causes structural flexibility and enhanced pore-filling by HTM film coated the perovskite layer [59]. Thus, a bigger Stokes shift is obtained when PL emission peak further moves towards higher wavelengths (visible area) via energy loss through radiative/non-radiative phenomena that lowers the emitted photons energy [60, 61].

Radiative emission PL peak has originated from recombination of charge carriers as an unwanted phenomenon in optoelectronic devices [62]. Therefore, less PL intensity with larger λ_{ss} are very useful for a PSC because a greater λ_{ss} indicates that the hole-electron recombination of less energy (i.e., minor recombination) occurs [63]. The highest λ_{ss} value of 18.54, 15.94, 15.77,

14.98, and 14.58 nm are achieved for the f-SFX-$CH_2C(O)SCF_3$, f-SFX-CF_3, f-SFX-SCF_3, f-SFX-CH_3, and f-SFX-OCF_3. However, lower values (λ_{ss}<12 nm) are obtained for other samples so that f-SFX-SCH_3 shows the smallest λ_{ss} =11.20 nm. Hence, it can be said that f-SFX-$CH_2C(O)SCF_3$ with the largest λ_{ss} is probably the best HTM among all samples studied.

Binding energy between hole and electron (E_b) can directly be correlated to the columbic interaction [64]. A smaller E_b validates a weaker columbic attraction, which leads to easier separation of charge carriers and improves PSC device efficiency. Table 5 presents E_1 and E_b values for all HTMs within dichloromethane solution. Besides, Fig. 8a displays E_b changes for the investigated HTMs. Apparently, E_b amounts vary from 0.454 eV (in f-SFX-OCF_3) to 0.563 eV (in f-SFX-CH_3). Notably, most of f-SFX-based HTMs reveal E_b values lower than E_b=0.51 eV for the Spiro-OMeTAD. Hence, it can be inferred that they can be desirable HTM samples for PSCs.

3.8. Reorganization energy

An improved hole mobility of HTM can result in bigger J_{SC} and FF for PSCs. Often, charge mobility is measured by hopping model for semiconductors [65]. Reorganization energy is known as a key factor in determination of charge hopping/transport in molecules and Marcus electron transfer theory is used to explain this parameter [66]. Reorganization energy is the energy necessary for deformation of structure and alteration of reactants and corresponding solvent particles. Reorganization energy includes internal reorganization (λ_{int}) and external polarization (λ_{ext}) [61]. λ_{int} exhibits variation of polarized geometry of atoms involved within transition from neutral to ionized state and vice versa. λ_{ext} explains variation of electronic polarization of adjacent molecules. It is hard to theoretically determine external contributors and consequently they are

usually ignored. Herein, we focus on λ_{int} to realize geometrical variations of molecules at neutral and ionic forms. Computed λ_h and λ_e for neutral, anionic, and cationic structures along with their excited states are measured and listed in Table 6. Moreover, Fig 8b graphically represents changes of λ_h and λ_e for all of the examined f-SFX-based HTMs.

According to Marcus electron-transfer concept, a larger hole/electron reorganization energy unveils that a slower hole/electron transport rate happens. It is seen in Table 6 and Fig. 8b that all λ_e values are greater than their related λ_h values, approving these substances are more promising HTMs instead of ETMs. Also, λ_h amounts alter from 0.047 eV (in f-SFX-$CH_2C(O)SH$) to 0.144 eV (in f-SFX-OCF_3). Therefore, f-SFX-OCF_3 needs the largest λ_h for geometry variation from neutral to cationic form as the biggest geometrical deformation occurs while the molecule changes from neutral to cationic state. Finally, f-SFX-$CH_2C(O)SH$ with the smallest λ_h may be introduced as the best HTM considering hole reorganization energies because a lower λ_h is expected to afford a larger hole mobility.

3.9. Charge transport integral and charge mobility

An improved hole mobility can accelerate transportation of holes. A molecular pair of the highest stability is utilized to evaluate charge mobility by hopping theory. Molecular pairs effectively provide transfer paths [67]. For this purpose, charge hopping rate (k_h or k_h) is calculated according to Marcus concept using Eq. (19) [68], where π=3.14 and T, $V_{h/e}$, and K_B are represented as room temperature (298 K), hole/electron transfer integral, and Boltzmann constant, respectively.

$$k = \frac{4\pi^2}{h} V^2 \frac{1}{\sqrt{4\pi\lambda k_B T}} exp\left[-\frac{\lambda}{4k_B T}\right] \quad (19)$$

Transfer integral is an influential parameter when estimating k_h or k_e. The V_h is obtained using HOMO-1 and HOMO energy splitting in two nearby particles, according to Energy Splitting in Dimer (ESID) methodology [69]. Additionally, V_e is estimated using LUMO+1 and LUMO orbitals in ESID methodology [70]. Hence, Eqs. (20) and (21) are used to achieve V_e and V_h, where E_H, $E_{(H-1)}$, E_L, and $E_{(L+1)}$ exhibit HOMO, HOMO-1, LUMO, and LUMO+1 energies, respectively. Table 6 exhibits that V_e and V_h values of f-SFX-based HTMs vary within ranges of 0.016-0.043 eV and 0.012-0.042 eV, respectively.

$$V_e = \frac{E_{L+1} - E_L}{2} \quad (20)$$

$$V_h = \frac{E_H - E_{H-1}}{2} \quad (21)$$

Hole and electron mobility (μ_h and μ_e) values are calculated using Eqs. (22) and (23) according to Einstein theory [71], where D is the diffusion coefficient, n shows dimensionality (n=3), r_i stands for centroid to centroid distance, and $p_m = k_m / \sum_m \quad k_m$,.

$$\mu_h \text{ or } \mu_e = \frac{e}{K_B T} D \quad (22)$$

$$D = \frac{1}{2n} \frac{\langle x(t)^2 \rangle}{t} \approx \frac{1}{2d} \sum_m \quad r_m^2 k_m p_m \quad (23)$$

Crystalline structures of HTMs are theoretically simulated through Polymorph module within Material Studio software [34]. This method is generally employed to simulate crystal structures of molecules [25]. All crystallographic data of HTMs are gathered in Table 7. Also, the most stable unit cells of f-SFX-based HTMs used for calculation of charge mobility are displayed in Fig. 9. The most stable crystalline structure with the lowest energy is applied to calculate charge mobility of each HTM. In all samples, the most stable structures belong to P-1 space group

except for the most stable structures of f-SFX-CH_3 and f-SFX-$CH_2C(O)SCH_3$ that belong to Cc and $P2_1$ space groups, respectively.

Fig. S4 demonstrates dimer structures of f-SFX-based HTMs used for hole mobility calculations. Table 8 affords centroid-to-centroid distance, electron- and hole-mobility (μ_e and μ_h), and electron- and hole-transfer rate (k_h, k_e) values for the f-SFX-based HTMs within dichloromethane. It is notable that smaller λ while larger V values are essential for higher charge mobility [72]. Hole mobility of an HTM has an important effect on J_{SC} and FF of PSC devices [73]. Therefore, it can be expected that larger J_{SC} and FF values are measured for PSCs fabricated with HTMs of larger μ_h values. There is a linear correlation between μ_e, μ_h and k_e, k_h values of HTMs, i.e. greater charge mobility is attained for the molecule indicating a bigger charge transfer rate. In all HTMs, k_h and μ_h are superior to their corresponding k_e and μ_e values, approving such materials are more auspicious hole transporters instead of electron transporters.

Evidently, f-SFX-$CH_2C(O)SH$, f-SFX-SCH_3, and f-SFX-CF_3 demonstrate the biggest k_h values of 4.835×10^{13}, 4.682×10^{13}, and 2.647×10^{13} s^{-1}, respectively. Moreover, the greatest μ_h amounts of 13.748, 12.876, and 7.817 $cm^2V^{-1}s^{-1}$ belong to f-SFX-$CH_2C(O)SH$, f-SFX-OCF_3, and f-SFX-SCF_3, respectively. Consequently, it can be decided that f-SFX-$CH_2C(O)SH$ can be an ideal HTM considering μ_h values.

It is noteworthy that all of the devised HTMs illustrate very much larger μ_h values that are almost 10^3-10^5 times higher than $\mu_{h\ (calculated)}$ $=5.65\times10^{-3}$ $cm^2V^{-1}s^{-1}$ and $\mu_{h\ (experimental)}$ $=4.53\times10^{-4}$ $cm^2V^{-1}s^{-1}$ of Spiro-OMeTAD [66]. Such surprising results prove that such compounds could be used as extremely favorable HTM candidates in high-performance PSC photovoltaics.

3.10. Photovoltaic parameters

V_{OC} is an important and substantial factor influencing the solar cell performance, which is the highest voltage when current density is zero [74]. For assessment of V_{OC} by Eq. (24), LUMO of acceptor and HOMO of donor are applied. Here, e indicates charge of electron (e=1) and 0.3 signifies a constant voltage decay.

$$V_{oc} = E_{LUMO\ of\ acceptor} - E_{HOMO\ of\ donor} - 0.3/e \qquad (24)$$

A lower HOMO energy of HTM results in a higher V_{OC} for the PSC because V_{OC} can be correlated to the difference between CB of SnO_2 ETM (-4.5 eV) [75] and HOMO level of HTM. Table 9 affords FF and V_{OC} values for the PSCs with SnO_2 ETM and the f-SFX-based HTMs. Noticeably, V_{OC} values vary very slightly in the range of 1.858-1.898 V, verifying the V_{OC} values of all HTMs are very comparable.

Fill factor is another critical parameter that affects the solar cell PCE [76]. Eq. (25) is employed to attain FF values for the devices with SnO_2 ETM and the f-SFX-based HTMs, in which T=298 K and K_B=8.617×10^{-5} shows the Boltzmann constant.

$$FF = \frac{\frac{e\,V_{OC}}{K_B\,T} - ln(\frac{e\,V_{OC}}{K_B\,T} + 0.72)}{\frac{e\,V_{OC}}{K_B\,T}+1} \qquad (25)$$

The calculated FFs for all HTMs are listed in Table 9. Furthermore, Fig. 10 reveals V_{OC} and FF variations of all HTMs calculated within dichloromethane solvent. Evidently, FF values of devised samples exhibit small deviations and change in the small range of 0.928-0.929 V. Notably, both of FF and V_{OC} values exactly unravel a similar variation trend.

All devices composed of the f-SFX-based HTMs illustrate FF=0.929 except for the f-SFX-CH_3 with FF=0.928. These FF values are bigger compared to those reported for PSCs containing

different SFX-containing HTMs [77-79]. Such outstanding results verify that all f-SFX-based samples devised here are very valuable HTMs. This is because the FF values of all HTMs are almost equal and their V_{OC} values are very comparable. However, it may be suggested that the candidates with V_{OC}≥1.895 V (including f-SFX-CF_3, f-SFX-$CH_2C(O)SCF_3$, f-SFX-OCF_3, f-SFX-SCF_3, and f-SFX-$CH_2C(O)OCF_3$) can be introduced as the most favorable HTMs for the PSC devices with SnO_2 ETM and $CsPbCl_3$ perovskite.

3.11. Temperature effect on HTM stability

In order to investigate the effect of temperature on stability of HTMs, which influences the PSC device stability, molecular dynamic simulations were performed on the unit cells of HTMs by NVT ensemble at two different temperatures including 298.15 and 318.15 K (25 and 45 °C). Fig. S5 presents energies of unit cells of SFX-based HTMs simulated at temperatures 298.15 and 318.15 K. It is observed that all energies including potential, kinetic, non-bond, and total energies of the f-SFX-based HTMs have reached equilibrium at the end of NVT simulations and show slight fluctuations, which confirm the cells are suitably relaxed at both examined temperatures. Moreover, all kinds of energies are larger at higher temperature (318.15 K) due to larger kinetic energy and easier molecular movements, which can increase the bond lengths and bond angles of molecules and their distances from each other. For example, Tables S2 reveals average total energies (kcal/mol) of simulated unit cells of the f-SFX-based HTMs at two temperatures, verifying effect of higher temperature on enhancement of total energy. Thus, it can be found that

the stability of HTM (and therefore the PSC device) decreases at higher temperature, particularly after long-term utilization of the solar cell.

3.12. Comparison with literature

Recently, four SFX derivatives were synthesized by attachment of amino N atom of bis(4-methoxyphenyl) amine (2PA) or *para*-carbon atom of phenyl group in bis(4-methoxyphenyl)phenyl amine (3PA) onto the *meta* and *para* (mp) or *meta* and *meta* (mm) positions of four phenyl rings of SFX unit [80]. The products were called mp-SFX-3PA, mp-SFX-2PA, mm-SFX-3PA, and mm-SFX-2PA, which were used as HTMs in PSCs fabricated with $CH_3NH_3PbI_3$ ($MAPbI_3$) perovskite, TiO_2 ETM, and Au back contact. The hole mobility values of the PSCs assembled using pristine mp-SFX-3PA, mm-SFX-3PA, mp-SFX-2PA, mm-SFX-2PA, and Spiro-OMeTAD were measured to be 4.0×10^{-6}, 5.3×10^{-6}, 3.0×10^{-5}, 8.7×10^{-6}, 4.5×10^{-6} $cm^2V^{-1}s^{-1}$, respectively. However, the μ_h values became larger after the HTMs were doped with lithium bis(trifluoromethylsulfonyl) imide (Li-TFSI) and 4-*tert*-butylpyridine (t-BP), which were equal to 3.3×10^{-5}, 2.2×10^{-5}, 1.5×10^{-4}, 9.9×10^{-5}, 2.0×10^{-5} $cm^2V^{-1}s^{-1}$, respectively, confirming they were enlarged by about 10 times compared to the un-doped samples. Obviously, the μ_h values of the f-SFX-based HTMs designed in our work are very much bigger (by approximately 10^5-10^7 times) than those of mp-SFX-3PA, mm-SFX-3PA, mp-SFX-2PA, mm-SFX-2PA, and Spiro-OMeTAD. This result approves that the f-SFX-based materials are able to be used as very powerful HTMs in practical PSCs fabrication and even in commercialization purposes.

Two SFX-based HTMs were synthesized and named X26 and X36 that were employed in fabrication of PSCs with mixed-ion perovskite ($[HC(NH_2)_2]_{0.85}(CH_3NH_3)_{0.15}Pb(I_{0.85}Br_{0.15})_3$), TiO_2

ETM, and Au back contact [77]. In both structures, there were two SFX units, onto which two bis(4-methoxyphenyl) amine groups were bound onto one phenyl ring of each SFX core while one 4-methoxyphenyl amine connected the two SFX unit together in X26 that was replaced by 1,1'-biphenyl-4,4'-bis(4-methoxyphenyl) amine in X36. The μ_h values of the X26, X36, and Spiro-OMeTAD HTMs doped with Li-TFSI and t-BP were 4.31×10^{-4}, 1.97×10^{-4}, 1.26×10^{-4} $cm^2V^{-1}s^{-1}$, respectively, specifying they were smaller by nearly 10^4-10^5 times compared to the f-SFX-based HTMs designed in this work.

Three HTMs were synthesized including SFXDA, *m*F-SFXDA, and *m*Cl-SFXDA, in which two bis(4-methoxyphenyl) amine, (4-methoxyphenyl) (4-methoxy-3-fluoro-phenyl) amine, and (4-methoxyphenyl) (4-methoxy-3-chloro-phenyl) amine, respectively, were attached onto two different phenyl rings of the central SFX core [81]. The μ_h values of the PSCs assembled using SnO_2 ETM, $Cs_{0.05}FA_{0.75}MA_{0.20}Pb(I_{0.96}Br_{0.04})_3$ perovskite (FA=formamidinium), Ag back contact, and SFXDA, *m*F-SFXDA, and *m*Cl-SFXDA doped with Li-TFSI and t-BP were 5.67×10^{-5}, 2.13×10^{-4}, 1.60×10^{-4} $cm^{2\ -1}s^{-1}$, respectively, specifying they were smaller by nearly 10^4-10^6 times compared to the f-SFX-based HTMs designed in our study.

In another work, four SFX-based HTMs were synthesized including 3',6'-bis(benzyloxy)-N2,N2,N7,N7-tetrakis(4-methoxyphenyl)spiro[fluorene-9,9'-xanthene]-2,7-diamine (XDB), N2,N2,N7,N7-tetrakis(4-methoxyphenyl)-3',6'-bis(pyridin-Z-ylmethoxy)spiro[fluorene-9,9'-xanthene]-2,7-diamine, where Z=2, 3, 4 for XOP, XMP, and XPP [82]. The *t*-BP-free PSC devices fabricated using SnO_2/C_{60} ETM, $MAPbI_3$ perovskite, Ag electrode, and XDB, XOP, XMP, XPP, and Spiro-OMeTAD HTMs doped with Li-TFSI and coated by MoO_3 layer exhibited hole mobility values of 7.3×10^{-5}, 9.7×10^{-5}, 1.3×10^{-4}, 1.6×10^{-4}, and 8.2×10^{-5} $cm^2V^{-1}s^{-1}$, respectively. Therefore, it is found

that the μ_h values obtained for the f-SFX-based HTMs are greater than those of XOP, XMP, XPP, and Spiro-OMeTAD (by almost 10^4-10^6 times).

The λ_h values for SFX-MeOTAD (SFX-1), HTM-FX' (SFX-2), SFX-3, and SFX-4 computed by DFT method at B3LYP/6-311G* level were measured to be 0.150, 0.197, 0.104, and 0.104 eV, respectively [83]. The average PCEs of the PSCs based on these HTMs, TO_2 ETM, and Au electrode were equal to 20.39, 19.45, 22.42, and 21.42%, respectively. Comparing these values with those of the f-SFX-based HTMs designed in this work reveals that the λ_h amounts (from 0.047 to 0.144 eV) are smaller, which led to higher V_{OC} and FF values fo the PSCs with the f-SFX-based HTMs.

DFT computations were carried out at the B3LYP-D3/6-31G (d,p) level of theory on the SFX-based HTMs functionalized with natural twenty-one amino acids that were attached from their carboxylic oxygen or amino nitrogen atoms at the *ortho*, *meta*, and *para* positions of two SFX phenyl rings to be used in PSCs with SnO_2 ETM, $FAPbI_3$ perovskite and Ag electrode [25]. It was found that the HTMs containing amino acid substitutions bond from N atoms instead of O atoms to the *para* positions had the most favorable HOMO levels. Also, the hole mobility values of such HTMs varied from 0.0018 $cm^2V^{-1}s^{-1}$ (in SFX-Serine) to 12.931 $cm^2V^{-1}s^{-1}$ (SFX-Leucine), verifying they were very much larger than those of Spiro-OMeTAD. Nonetheless, the μ_h values achieved in the current study (from 0.469 to 13.748 $cm^2V^{-1}s^{-1}$) are larger than all of the reported values. The V_{OC} and FF values of the amino acids-functionalized SFX samples were changed in the ranges of 0.378-0.916 V and 0.762-0.875, respectively. These values are smaller compared to those of the f-SFX-based HTMs (V_{OC}=1.858-1.898 V and FF=0.928-0.929), confirming the devised f-SFX-based samples are excellent HTM candidates for PSC photovoltaics.

4. Conclusions

Fifteen SFX-imidazole-sulfonylurea derivatives were designed as green and eco-friendly HTMs for PSCs to examine the effect of substituents on the optoelectronic and hole transfer properties of the designed HTMs. The architecture of the PSCs included SnO_2 as the ETM, $CsPbCl_3$ perovskite as the light harvesting material, and Ag electrode. DFT computations were accomplished to investigate electronic, optical, structural, and hole mobility characteristics of all compounds. FMO analysis proved that HOMO energy levels of all materials were suitably upper than that of $CsPbCl_3$ perovskite, verifying they were promising hole transporters. Chemical potential values of all f-SFX-based HTMs were larger compared to μ=-2.46 and -2.719 eV for X65 and Spiro-OMeTAD as standard HTMs, suggesting they were more stable than such well-known HTMs. All samples showed one broad peak accompanied by a shoulder within the wavelength range of 302.32-309.58 nm, validating their absorption peaks appeared in the UV spectral area, which were similar to the Spiro-OMeTAD with an absorption peak at λ_{abs}^{max}<400 nm, signifying they did not compete with the perovskite material for absorption of visible light. The λ_{em}^{max} values of the f-SFX-based materials changed from 317.13 nm (in f-SFX-H) to 325.50 nm (in f-SFX-$CH_2C(O)SCF_3$). E_b amounts varied from 0.454 eV (in f-SFX-OCF_3) to 0.563 eV (in f-SFX-CH_3) so that most HTMs had E_b values lower than E_b=0.51 eV for Spiro-OMeTAD, certifying a weaker electron-hole columbic attraction, easier separation of charge carriers, and improved PSC device efficiency. All λ_e values were greater than their related λ_h values, approving these substances were more promising HTMs instead of being ETMs. Moreover, λ_h amounts changed from 0.047 eV (in f-SFX-$CH_2C(O)SH$) to 0.144 eV (in f-SFX-OCF_3), substantiating f-SFX-$CH_2C(O)SH$ with the smallest λ_h might be the best HTM considering hole reorganization energies because a lower λ_h

could afford a larger hole mobility. The effect of temperature was investigated on stability of HTMs (which could influence the PSC device stability) using molecular dynamic simulations performed on the unit cells of HTMs by NVT ensemble at two different temperatures of 298.15 and 318.15 K (25 and 45 °C), confirming total energies of all systems were increased at higher temperature that could decrease the HTM and PSC device stability, particularly after long-term usage of the solar cell under intense environmental conditions. Also, all devices composed of the f-SFX-based HTMs demonstrated FF=0.929 except for the f-SFX-CH_3 with FF=0.928, indicating very much bigger FF values than those reported for PSCs containing different SFX-based HTMs. The greatest μ_h values of 13.748, 12.876, and 7.817 $cm^2V^{-1}s^{-1}$ belonged to f-SFX-$CH_2C(O)SH$, f-SFX-OCF_3, and f-SFX-SCF_3, respectively. Notably, all of the devised HTMs illustrated very much larger μ_h values that were almost 10^3-10^5 times higher than $\mu_{h\ (calculated)}$ =5.65×10^{-3} $cm^2V^{-1}s^{-1}$ and $\mu_{h\ (experimental)}$ =4.53×10^{-4} $cm^2V^{-1}s^{-1}$ of Spiro-OMeTAD, confirming they could be used as extremely favorable HTMs in high-performance PSC photovoltaics. In conclusion, the devised SFX-imidazole-sulfonylurea compounds could be applied as excellent low-cost, green, and eco-friendly HTMs to substitute the costly Spiro-OMeTAD material in PSC devices.

Acknowledgment

Authors gratefully thank computational facilities of Advanced Research Computing at Cardiff (ARCCA) Division, Cardiff University, and HPC Wales. By our membership in UK's HEC Materials Chemistry Consortium, funded by EPSRC (EP/R029431), also authors used ARCHER2 UK National Supercomputing Service (https://www.archer2.ac.uk). Besides, authors

thank High Performance Computing Research Center (HPCRC) at Amirkabir University of Technology for offering software and supercomputer facilities.

Conflicts of interest

The author declares that there are not any personal or financial conflicts of interest.

Data availability

The computational data will be delivered on request.

References

[1] Y. Shao, Y. Yuan, J. Huang, Correlation of energy disorder and open-circuit voltage in hybrid perovskite solar cells, Nature Energy 1(1) (2016) 15001.

[2] U. Khan, A. Rauf, S. Feng, A.R. Akbar, G. Peng, Q. Zheng, R. Wu, M. Khan, Z. Peng, F. Liu, Thermally stable and efficient CsF-doped All-Inorganic CsPbIBr2 perovskite solar cells exceeding 15% PCE, Inorganic Chemistry Communications 153 (2023) 110862.

[3] A. Mera, M.A. Rehman, Exploring the physical properties of Ae2TlCoF6 (Ae = Rb, Cs) double perovskites for solar cell applications by first-principles calculations, Inorganic Chemistry Communications 158 (2023) 111656.

[4] Z. Shariatinia, Z. Zolfaghari-Isavandi, Application of ZnxLayFezO4 spinel nanomaterial in quantum dot sensitized solar cells, Optik 212 (2020) 164682.

[5] S. Madani, T. Tesfamichael, H. Wang, N. Motta, Study of Pb-based and Pb-free perovskite solar cells using Cu-doped Ni1-xO thin films as hole transport material, Ceramics International 48(11) (2022) 15207-15217.

[6] M.A. Green, A. Ho-Baillie, Perovskite Solar Cells: The Birth of a New Era in Photovoltaics, ACS Energy Letters 2(4) (2017) 822-830.

[7] A. Mera, M. Awais Rehman, Z. ur Rehman, Z. Sarfraz, M. Sohaib, J. Fatima, M. Usman, Exploring the physical properties of Rb2TlSbM6 (M = Cl, Br) inorganic halide perovskites for solar cell applications: A DFT study, Inorganic Chemistry Communications 165 (2024) 112528.

[8] J. Sun, X. Yang, S. Sun, L. Zhao, S. Wang, Y. Li, Recent progress of rare earth conversion material in perovskite solar cells: A mini review, Inorganic Chemistry Communications 143 (2022) 109731.

[9] D. Gao, B. Qiao, Z. Xu, D. Song, P. Song, Z. Liang, Z. Shen, J. Cao, J. Zhang, S. Zhao, Postsynthetic, Reversible Cation Exchange between Pb2+ and Mn2+ in Cesium Lead Chloride Perovskite Nanocrystals, The Journal of Physical Chemistry C 121(37) (2017) 20387-20395.

[10] C. Dong, X. Jun, X. yang, Perovskite solar cell enhancement by tin oxide modification via doping sodium trifluoroacetate, Inorganic Chemistry Communications 167 (2024) 112776.

[11] S. Subramani, A.K. Ramasamy, G. Rajamanickam, A.K. Chauhan, R. Perumalsamy, Fabrication of ambient processed carbon-based inorganic silver bismuth iodide solar cells without any expensive hole transport materials, Inorganic Chemistry Communications 159 (2024) 111838.

[12] L. Noori, V. Hoseinpour, Z. Shariatinia, Optimization of TiO2 paste concentration employed as electron transport layers in fully ambient air processed perovskite solar cells with a low-cost architecture, Ceramics International 48(1) (2022) 320-336.

[13] D.G. Lee, M.-c. Kim, S. Wang, B.J. Kim, Y.S. Meng, H.S. Jung, Effect of Metal Electrodes on Aging-Induced Performance Recovery in Perovskite Solar Cells, ACS Applied Materials & Interfaces 11(51) (2019) 48497-48504.

[14] R. Chen, W. Zhang, X. Guan, H. Raza, S. Zhang, Y. Zhang, P.A. Troshin, S.A. Kuklin, Z. Liu, W. Chen, Rear Electrode Materials for Perovskite Solar Cells, Advanced Functional Materials 32(26) (2022) 2200651.

[15] W. Ming, D. Yang, T. Li, L. Zhang, M.-H. Du, Formation and Diffusion of Metal Impurities in Perovskite Solar Cell Material CH3NH3PbI3: Implications on Solar Cell Degradation and Choice of Electrode, Advanced Science 5(2) (2018) 1700662.

[16] G.F.I. Toki, M.K. Hossain, M. Shihab Uddin, A.M. Tawfeek, S. Rabhi, M.A. Darwish, R. Haldhar, D.K. Dwivedi, J. Madan, R. Pandey, Unveiling the potential of lead-free Cs2AgBi0.75Sb0.25Br6 double perovskite solar cells with multilayer charge transport for 30% efficiency, Inorganic Chemistry Communications 165 (2024) 112439.

[17] C.-D. Si, X.-D. Lv, S.-J. Long, Perovskite solar cells employing copper (I/II) porphyrin hole-transport material with enhanced performance, Inorganic Chemistry Communications 112 (2020) 107701.

[18] Z. Yu, L. Sun, Recent Progress on Hole-Transporting Materials for Emerging Organometal Halide Perovskite Solar Cells, Advanced Energy Materials 5(12) (2015) 1500213.

[19] L. Zhu, J. Xiao, J. Shi, J. Wang, S. Lv, Y. Xu, Y. Luo, Y. Xiao, S. Wang, Q. Meng, X. Li, D. Li, Efficient CH3NH3PbI3 perovskite solar cells with 2TPA-n-DP hole-transporting layers, Nano Research 8(4) (2015) 1116-1127.

[20] J. Burschka, A. Dualeh, F. Kessler, E. Baranoff, N.-L. Cevey-Ha, C. Yi, M.K. Nazeeruddin, M. Grätzel, Tris(2-(1H-pyrazol-1-yl)pyridine)cobalt(III) as p-Type Dopant for Organic Semiconductors and Its Application in Highly Efficient Solid-State Dye-Sensitized Solar Cells, Journal of the American Chemical Society 133(45) (2011) 18042-18045.

[21] U. Bach, D. Lupo, P. Comte, J.E. Moser, F. Weissörtel, J. Salbeck, H. Spreitzer, M. Grätzel, Solid-state dye-sensitized mesoporous TiO2 solar cells with high photon-to-electron conversion efficiencies, Nature 395(6702) (1998) 583-585.

[22] L. Peter, “Sticky Electrons” Transport and Interfacial Transfer of Electrons in the Dye-Sensitized Solar Cell, Accounts of Chemical Research 42(11) (2009) 1839-1847.

[23] F. Fabregat-Santiago, J. Bisquert, L. Cevey, P. Chen, M. Wang, S.M. Zakeeruddin, M. Grätzel, Electron Transport and Recombination in Solid-State Dye Solar Cell with Spiro-OMeTAD as Hole Conductor, Journal of the American Chemical Society 131(2) (2009) 558-562.

[24] N. Cocherel, C. Poriel, L. Vignau, J.-F. Bergamini, J. Rault-Berthelot, DiSpiroXanthene-IndenoFluorene: A New Blue Emitter for Nondoped Organic Light Emitting Diode Applications, Organic Letters 12(3) (2010) 452-455.

[25] H. Askari, Z. Shariatinia, S. Sarabadani-Tafreshi, N.H. de Leeuw, Remarkable hole transport properties of Spiro[fluorene-9,9′-xanthene] derivatives containing natural amino acid substituents for perovskite photovoltaics, Solar Energy 269 (2024) 112308.

[26] P. Anastas, N. Eghbali, Green chemistry: principles and practice, Chemical Society Reviews 39(1) (2010) 301-312.

[27] M. Irimia-Vladu, "Green" electronics: biodegradable and biocompatible materials and devices for sustainable future, Chemical Society Reviews 43(2) (2014) 588-610.

[28] L.-H. Xie, F. Liu, C. Tang, X.-Y. Hou, Y.-R. Hua, Q.-L. Fan, W. Huang, Unexpected One-Pot Method to Synthesize Spiro[fluorene-9,9‘-xanthene] Building Blocks for Blue-Light-Emitting Materials, Organic Letters 8(13) (2006) 2787-2790.

[29] G. Elmacı, E. Aktan, N. Seferoğlu, T. Hökelek, Z. Seferoğlu, Synthesis, molecular structure and computational study of (Z)-2-((E)-4-nitrobenzylidene)hydrazone)-1,2-diphenylethan-1-one, Journal of Molecular Structure 1099 (2015) 83-91.

[30] G. Elmacı, H. Duyar, B. Aydıner, I. Yahaya, N. Seferoğlu, E. Şahin, S.P. Çelik, L. Açık, Z. Seferoğlu, Novel benzildihydrazone based Schiff bases: Syntheses, characterization, thermal properties, theoretical DFT calculations and biological activity studies, Journal of Molecular Structure 1184 (2019) 271-280.

[31] G. Elmacı, H. Duyar, B. Aydıner, N. Seferoğlu, M.A. Naziri, E. Şahin, Z. Seferoğlu, The syntheses, molecular structure analyses and DFT studies on new benzil monohydrazone based Schiff bases, Journal of Molecular Structure 1162 (2018) 37-44.

[32] M. Frisch, Gaussian 03 rev. E. 01, http://www. gaussian. com/ (2004).

[33] M. Vatanparast, Z. Shariatinia, Isoindigo derivatives as promising hole transport materials for perovskite solar cells, Solar Energy 230 (2021) 260-268.

[34] D. ACCELRYS, Visualizer Version 2.0, ACCELRYS Software Inc., San Diego (2009).

[35] N. Hernández-Haro, J. Ortega-Castro, Y.B. Martynov, R.G. Nazmitdinov, A. Frontera, DFT prediction of band gap in organic-inorganic metal halide perovskites: An exchange-correlation functional benchmark study, Chemical Physics 516 (2019) 225-231.

[36] L. Kronik, T. Stein, S. Refaely-Abramson, R. Baer, Excitation gaps of finite-sized systems from optimally tuned range-separated hybrid functionals, Journal of Chemical Theory and Computation 8(5) (2012) 1515-1531.

[37] E. Kraisler, L. Kronik, Piecewise linearity of approximate density functionals revisited: Implications for frontier orbital energies, Physical review letters 110(12) (2013) 126403.

[38] Y. Tao, K. Yuan, T. Chen, P. Xu, H. Li, R. Chen, C. Zheng, L. Zhang, W. Huang, Thermally activated delayed fluorescence materials towards the breakthrough of organoelectronics, Advanced materials 26(47) (2014) 7931-7958.

[39] S. Naqvi, A. Patra, Hole transport materials for perovskite solar cells: a computational study, Materials Chemistry and Physics 258 (2021) 123863.

[40] C.-G. Zhan, J.A. Nichols, D.A. Dixon, Ionization potential, electron affinity, electronegativity, hardness, and electron excitation energy: molecular properties from density functional theory orbital energies, The Journal of Physical Chemistry A 107(20) (2003) 4184-4195.

[41] Z. Li, Y. Yun, H. Huang, Z. Ding, X. Li, B. Zhao, W. Huang, Fluorine substitution position effects on spiro(fluorene-9,9’-xanthene) cored hole transporting materials for high-performance planar perovskite solar cells, Journal of Energy Chemistry 57 (2021) 341-350.

[42] L. Zhang, X.-M. Peng, G.L.V. Damu, R.-X. Geng, C.-H. Zhou, Comprehensive Review in Current Developments of Imidazole-Based Medicinal Chemistry, Medicinal Research Reviews 34(2) (2014) 340-437.

[43] P.M. Thulé, G. Umpierrez, Sulfonylureas: a new look at old therapy, Current diabetes reports 14 (2014) 1-8.

[44] Z.-Z. Sun, Y.-L. Xu, R. Zhu, H.-Y. Liu, How to stabilize the HOMO levels and to improve the charge transport properties of hole-transporting materials? Probing the effects of molecular symmetry, Organic Electronics 63 (2018) 86-92.

[45] L.K. Ono, Z. Hawash, E.J. Juarez-Perez, L. Qiu, Y. Jiang, Y. Qi, The influence of secondary solvents on the morphology of a spiro-MeOTAD hole transport layer for lead halide perovskite solar cells, Journal of Physics D: Applied Physics 51(29) (2018) 294001.

[46] S.H. Lee, S.B. Lim, J.Y. Kim, S. Lee, S.Y. Oh, G.M. Kim, An Alternative to Chlorobenzene as a Hole Transport Materials Solvent for High-Performance Perovskite Solar Cells, Crystals 13(12) (2023) 1667.

[47] Z. Shariatinia, How does changing substituents affect the hole transport characteristic of butterfly-shaped materials based on fluorene–dithiophene core for perovskite photovoltaics, Journal of Industrial and Engineering Chemistry 118 (2023) 280-297.

[48] J. Ho, A. Klamt, M.L. Coote, Comment on the correct use of continuum solvent models, The journal of physical chemistry A 114(51) (2010) 13442-13444.

[49] M.L. Petrus, K. Schutt, M.T. Sirtl, E.M. Hutter, A.C. Closs, J.M. Ball, J.C. Bijleveld, A. Petrozza, T. Bein, T.J. Dingemans, New Generation Hole Transporting Materials for Perovskite Solar Cells: Amide-Based Small-Molecules with Nonconjugated Backbones, Advanced Energy Materials 8(32) (2018) 1801605.

[50] H.C. Liao, T.L.D. Tam, P. Guo, Y. Wu, E.F. Manley, W. Huang, N. Zhou, C.M.M. Soe, B. Wang, M.R. Wasielewski, Dopant-free hole transporting polymers for high efficiency, environmentally stable perovskite solar cells, Advanced Energy Materials 6(16) (2016) 1600502.

[51] L. Andrews, A. Citra, Infrared spectra and density functional theory calculations on transition metal nitrosyls. Vibrational frequencies of unsaturated transition metal nitrosyls, Chemical reviews 102(4) (2002) 885-912.

[52] Z. Shariatinia, A. Barzegari, 22 - Polysaccharide hydrogel films/membranes for transdermal delivery of therapeutics, in: S. Maiti, S. Jana (Eds.), Polysaccharide Carriers for Drug Delivery, Woodhead Publishing2019, pp. 639-684.

[53] Z. Shariatinia, Chapter 2 - Pharmaceutical applications of natural polysaccharides, in: M.S. Hasnain, A.K. Nayak (Eds.), Natural Polysaccharides in Drug Delivery and Biomedical Applications, Academic Press2019, pp. 15-57.

[54] K. Gholivand, M. Pourayoubi, Z. Shariatinia, 2,3J(P,X) [X=H, C] coupling constants dependency on the ring size, hybridization and substituents in new diazaphospholes and diazaphosphorinanes, NMR and X-ray crystallography studies, Polyhedron 26(4) (2007) 837-844.

[55] S. Gul, K.M. Katubi, I.A. Bhatti, J. Iqbal, M. Al-Buriahi, S. Alomairy, Tuning the photovoltaic parameters of spiro [fluorenexanthene]-diol (SFX-OH)-based crosslinked donor materials for efficient organic solar cells, Computational and Theoretical Chemistry 1214 (2022) 113778.

[56] M. Shafiq, M.B. Tahir, B. Ahmed, A. Dahshan, H.E. Ali, M. Sagir, DFT screening of Ga-dopped ScInO3 perovskite for optoelectronic and solar cell applications, Inorganic Chemistry Communications 161 (2024) 112054.

[57] A. Algahtani, Amina, F. Rehman, M. Liaqat, N. Juraev, I. Khan, A.M. Alsuhaibani, Abdullah, V. Tirth, M.S. Refat, A. Zaman, Probing the physical properties of Sr3AsX3 (X = F and Br) perovskite compounds for prospective solar cell applications employing the DFT framework, Inorganic Chemistry Communications 162 (2024) 112186.

[58] P. Qin, H. Kast, M.K. Nazeeruddin, S.M. Zakeeruddin, A. Mishra, P. Bäuerle, M. Grätzel, Low band gap S,N-heteroacene-based oligothiophenes as hole-transporting and light absorbing materials for efficient perovskite-based solar cells, Energy & Environmental Science 7(9) (2014) 2981-2985.

[59] K. Wang, Q. Wang, X. Chen, G. Ji, Efficient strategies to improve the performance of 6,12-dihydroindeno[1,2-b]fluorine core based hole transport materials, Solar Energy 217 (2021) 93-104.

[60] F. Abbas, M.D. Mohammadi, H. Louis, I.O. Amodu, D.E. Charlie, T.E. Gber, Design of new bithieno thiophene (BTTI) central core-based small molecules as efficient hole transport materials for perovskite solar cells and donor materials for organic solar cells, Materials Science and Engineering: B 291 (2023) 116392.

[61] J.-L. Brédas, D. Beljonne, V. Coropceanu, J. Cornil, Charge-transfer and energy-transfer processes in π-conjugated oligomers and polymers: a molecular picture, Chemical reviews 104(11) (2004) 4971-5004.

[62] A. Alizadeh, Z. Shariatinia, Unveiling the influence of SmFeO3-TiO2 nanocomposites as high performance photoanodes of dye-sensitized solar cells, Journal of Molecular Liquids (2021) 118070.

[63] J.M. Dos Santos, L.K. Jagadamma, M. Cariello, I.D. Samuel, G. Cooke, A BODIPY small molecule as hole transporting material for efficient perovskite solar cells, Sustainable Energy & Fuels 6(18) (2022) 4322-4330.

[64] Z. Zolfaghari-Isavandi, Z. Shariatinia, Fabrication of CdS quantum dot sensitized solar cells using nitrogen functionalized CNTs/TiO2 nanocomposites, Diamond and Related Materials 81 (2018) 1-15.

[65] L. Wang, D. Beljonne, Charge transport in organic semiconductors: Assessment of the mean field theory in the hopping regime, The Journal of Chemical Physics 139(6) (2013).

[66] W.-J. Chi, Q.-S. Li, Z.-S. Li, Exploring the electrochemical properties of hole transport materials with spiro-cores for efficient perovskite solar cells from first-principles, Nanoscale 8(11) (2016) 6146-6154.

[67] M.M. Elnaggar, L.G. Gutsev, N.A. Emelianov, P.M. Kuznetsov, L.A. Frolova, S.M. Aldoshin, P.A. Troshin, Molecular Engineering of Polytriarylamine-Based Hole-Transport Materials for p–i–n Perovskite Solar Cells: Methyl Groups Matter, ACS Applied Energy Materials 5(5) (2022) 5388-5394.

[68] R.A. Marcus, Chemical and electrochemical electron-transfer theory, Annual review of physical chemistry 15(1) (1964) 155-196.

[69] M. Pope, C.E. Swenberg, Electronic processes in organic crystals and polymers, Oxford university press1999.

[70] T.P. Nguyen, J.H. Shim, J.Y. Lee, Density Functional Theory Studies of Hole Mobility in Picene and Pentacene Crystals, The Journal of Physical Chemistry C 119(21) (2015) 11301-11310.

[71] J. Xiao, H.-J. Yu, D. Wang, W.-J. Gao, A. Shinohara, J. Xia, G. Shao, An Acetylene-Linked 9,9'-Bicarbazole-Based Hole-Transporting Material for Efficient Perovskite Solar Cells, Energy & Fuels 36(4) (2022) 2086-2094.

[72] W.-Q. Deng, W.A. Goddard, Predictions of Hole Mobilities in Oligoacene Organic Semiconductors from Quantum Mechanical Calculations, The Journal of Physical Chemistry B 108(25) (2004) 8614-8621.

[73] K.-M. Lee, Y.-S. Huang, W.-H. Chiu, Y.-K. Huang, G. Chen, G.B. Adugna, S.-R. Li, F.-J. Lin, S.-I. Lu, H.-C. Hsieh, K.-L. Liau, C.-C. Huang, Y. Tai, Y.-T. Tao, Y.-D. Lin, Fluorinated Pentafulvalene-

Fused Hole-Transporting Material Enhances the Performance of Perovskite Solar Cells with Efficiency Exceeding 23%, Advanced Functional Materials 33(48) (2023) 2306367.

[74] E. Jalali-Moghadam, Z. Shariatinia, Quantum dot sensitized solar cells fabricated by means of a novel inorganic spinel nanoparticle, Applied Surface Science 441 (2018) 1-11.

[75] L. Xiong, Y. Guo, J. Wen, H. Liu, G. Yang, P. Qin, G. Fang, Review on the Application of SnO2 in Perovskite Solar Cells, Advanced Functional Materials 28(35) (2018) 1802757.

[76] F. Ziaeifar, A. Alizadeh, Z. Shariatinia, Dye sensitized solar cells fabricated based on nanocomposite photoanodes of TiO2 and AlMo0.5O3 perovskite nanoparticles, Solar Energy 218 (2021) 435-444.

[77] J. Zhang, B. Xu, L. Yang, C. Ruan, L. Wang, P. Liu, W. Zhang, N. Vlachopoulos, L. Kloo, G. Boschloo, L. Sun, A. Hagfeldt, E.M.J. Johansson, The Importance of Pendant Groups on Triphenylamine-Based Hole Transport Materials for Obtaining Perovskite Solar Cells with over 20% Efficiency, Advanced Energy Materials 8(2) (2018) 1701209.

[78] Y. Fu, Y. Li, Q. Zeng, H. Wu, L. Wang, H. Tang, G. Xing, D. Cao, Influence of donor units on spiro[fluorene-9,9’-xanthene]-based dopant-free hole transporting materials for perovskite solar cells, Solar Energy 216 (2021) 180-187.

[79] B. Xu, D. Bi, Y. Hua, P. Liu, M. Cheng, M. Grätzel, L. Kloo, A. Hagfeldt, L. Sun, A low-cost spiro[fluorene-9,9’-xanthene]-based hole transport material for highly efficient solid-state dye-sensitized solar cells and perovskite solar cells, Energy & Environmental Science 9(3) (2016) 873-877.

[80] K. Liu, Y. Yao, J. Wang, L. Zhu, M. Sun, B. Ren, L. Xie, Y. Luo, Q. Meng, X. Zhan, Spiro[fluorene-9,9’-xanthene]-based hole transporting materials for efficient perovskite solar cells with enhanced stability, Materials Chemistry Frontiers 1(1) (2017) 100-110.

[81] Z. Zhang, L. Shen, S. Wang, L. Zheng, D. Li, Z. Li, Y. Xing, K. Guo, L. Xie, Z. Wei, Halogenated Hole-Transport Molecules with Enhanced Isotropic Coordination Capability Enable Improved Interface and Light Stability of Perovskite Solar Cells, Advanced Energy Materials 13(14) (2023) 2204362.

[82] B. Xu, Z. Zhu, J. Zhang, H. Liu, C.-C. Chueh, X. Li, A.K.-Y. Jen, 4-Tert-butylpyridine Free Organic Hole Transporting Materials for Stable and Efficient Planar Perovskite Solar Cells, Advanced Energy Materials 7(19) (2017) 1700683.

[83] M. Han, X. Zhang, X. Liu, R. Ghadari, N. Wu, H. Quan, B. Li, W. Du, S. Dai, Substitution Position Effects on Spiro[Fluorene-9,9'-Xanthene]-Diphenylamine Hole-Transporting Materials for Perovskite Solar Cells, Solar RRL 8(1) (2024) 2300824.

Table 1. FMOs and E_g energies of HTM samples in dichloromethane solvent comprising imidazole-sulfonylurea moieties bound to *para*-carbon atoms of two six-membered rings of SFX core, onto which various 15 substituents are attached.

No.	HTM[a]	E(HOMO) (eV)	E(LUMO) (eV)	E_g (eV)
1	f-SFX-$CH_2C(O)OH$	-5.985	-1.609	4.38
2	f-SFX-H	-5.990	-1.616	4.37
3	f-SFX-SH	-5.992	-1.652	4.34
4	f-SFX-OH	-5.994	-1.651	4.34
5	f-SFX-OCH_3	-5.993	-1.653	4.34
6	f-SFX-$CH_2C(O)OCH_3$	-5.983	-1.608	4.37
7	f-SFX-CH_3	-5.958	-1.533	4.43
8	f-SFX-SCH_3	-5.991	-1.646	4.34
9	f-SFX-$CH_2C(O)SCH_3$	-5.987	-1.624	4.36
10	f-SFX-$CH_2C(O)SH$	-5.994	-1.643	4.35
11	f-SFX-OCF_3	-5.997	-1.712	4.28
12	f-SFX-$CH_2C(O)OCF_3$	-5.995	-1.653	4.34
13	f-SFX-CF_3	-5.998	-1.695	4.30
14	f-SFX-SCF_3	-5.997	-1.690	4.31
15	f-SFX-$CH_2C(O)SCF_3$	-5.998	-1.664	4.33
16	Spiro-OMeTAD	-4.501	-.937	3.56

[a]f-SFX=SFX-Imidazole-Sulfonylurea, where f-SFX means functionalized SFX.

Table 2. Dipole moments (within gas phase and CH_2Cl_2 solution), ΔG_{solv}, AIP, AEA, and $E_{binding}$ within dichloromethane solvent calculated.

HTM	ΔG_{solv} (kcal/mol)	dipole moment in solvent (Debye)	dipole moment in gas phase (Debye)	AEA (eV)	AIP (eV)	$E_{binding}$ (kcal/mol)
f-SFX-$CH_2C(O)OH$	-36.995	19.82	13.95	-1.833	5.965	-12468.06
f-SFX-H	-35.306	20.86	14.40	-1.833	5.970	-11120.16
f-SFX-SH	-35.040	18.16	13.74	-1.898	5.977	-11193.03
f-SFX-OH	-20.599	21.24	13.07	-1.898	5.980	-11236.08
f-SFX-OCH_3	-35.218	20.93	14.83	-1.900	5.980	-11816.49
f-SFX-$CH_2C(O)OCH_3$	-35.471	18.13	13.79	-1.828	5.962	-13044.88
f-SFX-CH_3	-29.610	16.25	10.97	-1.758	5.900	-11710.62
f-SFX-SCH_3	-34.283	17.38	12.80	-1.889	5.973	-11791.31
f-SFX-$CH_2C(O)SCH_3$	-35.922	19.50	14.31	-1.852	5.969	-12944.10
f-SFX-$CH_2C(O)SH$	-37.429	23.30	14.70	-1.882	5.979	-12349.55
f-SFX-OCF_3	-21.641	19.45	14.49	-2.708	5.988	-11918.22
f-SFX-$CH_2C(O)OCF_3$	-35.186	25.40	16.58	-1.892	5.980	-13134.21
f-SFX-CF_3	-34.087	21.05	16.81	-2.713	5.988	-11791.59

f-SFX-SCF_3	-34.081	22.68	17.44	-2.664	5.986	-11860.94
f-SFX-$CH_2C(O)SCF_3$	-38.555	27.11	16.99	-1.912	5.986	-13009.87

Table 3. Molecular descriptors including μ, η, S, χ, ω, and ΔN_{max} computed for HTM molecules.

HTM	μ (eV)	η (eV)	S (eV)	χ (eV)	ω (eV)	ΔN_{max}
f-SFX-$CH_2C(O)OH$	-3.797	2.188	0.457	3.797	3.295	1.736
f-SFX-H	-3.803	2.187	0.457	3.803	3.307	1.739
f-SFX-SH	-3.822	2.170	0.461	3.822	3.366	1.761
f-SFX-OH	-3.823	2.172	0.461	3.823	3.364	1.760
f-SFX-OCH_3	-3.823	2.170	0.461	3.823	3.367	1.761
f-SFX-$CH_2C(O)OCH_3$	-3.796	2.187	0.457	3.796	3.293	1.735
f-SFX-CH_3	-3.745	2.213	0.452	3.745	3.170	1.693
f-SFX-SCH_3	-3.819	2.172	0.460	3.819	3.356	1.758
f-SFX-$CH_2C(O)SCH_3$	-3.806	2.182	0.458	3.806	3.319	1.744
f-SFX-$CH_2C(O)SH$	-3.819	2.175	0.460	3.819	3.352	1.755
f-SFX-OCF_3	-3.854	2.142	0.467	3.854	3.467	1.799
f-SFX-$CH_2C(O)OCF_3$	-3.824	2.171	0.461	3.824	3.368	1.762
f-SFX-CF_3	-3.846	2.151	0.465	3.846	3.439	1.788
f-SFX-SCF_3	-3.843	2.154	0.464	3.843	3.429	1.785

f-SFX-$CH_2C(O)SCF_3$	-3.831	2.167	0.461	3.831	3.386	1.768
Spiro-OMeTAD	-2.719	1.782	0.561	2.719	2.075	1.526

Table 4. Calculated λ^{max}_{abs}, main transition in absorption spectra (transition probability), f_{abs}^{max}, λ^{max}_{em}, λ_{ss}, and LHE for all SFX-based HTMs.

HTM	λ_{abs}^{max} (nm)	Main transition in absorption spectra (transition probability)[a]	f_{abs}^{max}	λ_{em}^{max} (nm)	λ_{ss} (nm)	LHE
f-SFX-$CH_2C(O)OH$	305.56	H-1→L+1 (31.87%)	0.3494	317.19	11.63	0.553
f-SFX-H	305.64	H-1→L+1 (32.66%)	0.3517	317.13	11.49	0.555
f-SFX-SH	307.59	H-1→L+1 (32.63%)	0.3238	318.82	11.23	0.526
f-SFX-OH	306.47	H-1→L+1 (43.31%)	0.3622	318.40	11.93	0.420
f-SFX-OCH_3	306.64	H-1→L+1 (37.77%)	0.3141	318.49	11.85	0.481

f-SFX-$CH_2C(O)OCH_3$	305.69	H-1→L+1 (35.68%)	0.3980	317.34	11.65	0.600
f-SFX-CH_3	302.32	H→L+1 (40.53%)	0.5938	317.30	14.98	0.404
f-SFX-SCH_3	307.27	H-1→L+1 (37.17%)	0.3676	318.47	11.20	0.571
f-SFX-$CH_2C(O)SCH_3$	306.31	H-1→L+1 (34.36%)	0.3732	317.72	11.41	0.577
f-SFX-$CH_2C(O)SH$	306.16	H-1→L+1 (43.45%)	0.3986	318.12	11.96	0.417
f-SFX-OCF_3	309.58	H-1→L+1 (55.36%)	0.4224	324.16	14.58	0.622
f-SFX-$CH_2C(O)OCF_3$	306.70	H-1→L+1 (41.06%)	0.3644	318.53	11.83	0.454
f-SFX-CF_3	308.71	H-1→L+1 (53.64%)	0.4200	324.65	15.94	0.620
f-SFX-SCF_3	309.26	H-1→L+1 (33.80%)	0.3032	325.03	15.77	0.486
f-SFX-$CH_2C(O)SCF_3$	306.96	H-1→L+1 (49.94%)	0.4303	325.50	18.54	0.351

[a]H=HOMO, L=LUMO.

Table 5. E_1 and E_b values computed in dichloromethane solution.

HTM	E_1 (eV)	E_b (eV)
f-SFX-$CH_2C(O)OH$	3.848	0.528
f-SFX-H	3.847	0.527
f-SFX-SH	3.842	0.498
f-SFX-OH	3.843	0.500
f-SFX-OCH_3	3.842	0.499
f-SFX-$CH_2C(O)OCH_3$	3.848	0.527
f-SFX-CH_3	3.863	0.563
f-SFX-SCH_3	3.842	0.503
f-SFX-$CH_2C(O)SCH_3$	3.845	0.518
f-SFX-$CH_2C(O)SH$	3.843	0.508
f-SFX-OCF_3	3.831	0.454
f-SFX-$CH_2C(O)OCF_3$	3.841	0.501
f-SFX-CF_3	3.834	0.468
f-SFX-SCF_3	3.837	0.471
f-SFX-$CH_2C(O)SCF_3$	3.840	0.495

Table 6. The λ_h, λ_e, V_h, and V_e obtained for HTM molecules.

HTM	λ_h (eV)	λ_e (eV)	V_h (eV)	V_e (eV)
f-SFX-$CH_2C(O)OH$	0.094	0.596	0.026	0.025
f-SFX-H	0.094	0.571	0.025	0.025
f-SFX-SH	0.099	0.653	0.032	0.020
f-SFX-OH	0.101	0.666	0.033	0.020
f-SFX-OCH_3	0.100	0.677	0.033	0.020
f-SFX-$CH_2C(O)OCH_3$	0.094	0.584	0.025	0.026
f-SFX-CH_3	0.105	0.639	0.012	0.043
f-SFX-SCH_3	0.047	0.646	0.031	0.021
f-SFX-$CH_2C(O)SCH_3$	0.095	0.607	0.027	0.024
f-SFX-$CH_2C(O)SH$	0.047	0.639	0.031	0.022
f-SFX-OCF_3	0.144	0.836	0.042	0.016
f-SFX-$CH_2C(O)OCF_3$	0.010	0.639	0.032	0.021
f-SFX-CF_3	0.111	0.701	0.039	0.017
f-SFX-SCF_3	0.107	0.558	0.037	0.017
f-SFX-$CH_2C(O)SCF_3$	0.103	0.695	0.035	0.020

Table 7. Crystallographic data of the most stable HTM crystal structures.

HTM	Space group	Length a (Å)	Length b (Å)	Length c (Å)	Angle α (°)	Angle β (°)	Angle γ (°)
f-SFX-$CH_2C(O)OH$	P-1	18.998	8.115	20.100	62.759	118.139	117.179
f-SFX-H	P-1	12.452	9.956	18.859	65.054	78.165	74.015
f-SFX-SH	P-1	20.464	9.342	12.741	107.405	95.602	82.242
f-SFX-OH	P-1	8.488	23.260	12.201	86.021	69.478	58.041
f-SFX-OCH_3	P-1	19.691	8.678	16.979	124.230	68.107	108.417
f-SFX-$CH_2C(O)OCH_3$	P-1	20.661	15.577	13.882	107.326	73.321	142.739
f-SFX-CH_3	CC	37.588	17.626	7.550	90.000	118.156	90.000
f-SFX-SCH_3	P-1	13.231	21.113	9.837	110.452	115.237	92.119
f-SFX-$CH_2C(O)SCH_3$	$P2_1$	23.019	19.632	8.038	90.000	45.929	90.000
f-SFX-$CH_2C(O)SH$	P-1	19.400	14.912	9.094	81.556	86.309	106.413
f-SFX-OCF_3	P-1	29.376	12.568	9.455	106.819	114.955	110.977

f-SFX-$CH_2C(O)OCF_3$	P-1	14.320	9.944	21.114	81.730	80.320	60.900
f-SFX-CF_3	P-1	18.760	9.921	12.696	100.847	101.402	82.576
f-SFX-SCF_3	P-1	9.889	19.958	12.866	81.511	108.910	82.953
f-SFX-$CH_2C(O)SCF_3$	P-1	13.891	9.740	20.964	85.920	95.032	110.948

Table 8. The r, k_h, k_e, μ_h, and μ_e values of HTMs within CH_2Cl_2 solution.

HTM	r (Å)	k_h (s^{-1})	k_e (s^{-1})	μ_h ($cm^2V^{-1}s^{-1}$)	μ_e ($cm^2V^{-1}s^{-1}$)
f-SFX-$CH_2C(O)OH$	17.289	1.454×10^{13}	4.186×10^{10}	2.801	0.008
f-SFX-H	19.192	1.425×10^{13}	5.600×10^{10}	3.382	0.013
f-SFX-SH	7.430	2.060×10^{13}	1.505×10^{10}	0.733	0.001
f-SFX-OH	16.648	2.168×10^{13}	1.272×10^{10}	3.873	0.002
f-SFX-OCH_3	13.912	2.157×10^{13}	1.172×10^{10}	2.691	0.002

f-SFX-$CH_2C(O)OCH_3$	19.202	1.332×10^{13}	5.217×10^{10}	3.167	0.012
f-SFX-CH_3	16.623	2.635×10^{12}	7.916×10^{10}	0.469	0.014
f-SFX-SCH_3	7.610	4.682×10^{13}	1.779×10^{10}	1.748	0.001
f-SFX-$CH_2C(O)SCH_3$	21.841	1.609×10^{13}	3.488×10^{10}	4.948	0.011
f-SFX-$CH_2C(O)SH$	21.004	4.835×10^{13}	2.002×10^{10}	13.748	0.006
f-SFX-OCF_3	32.324	1.912×10^{13}	1.486×10^{9}	12.876	0.001
f-SFX-$CH_2C(O)OCF_3$	21.450	2.061×10^{13}	1.939×10^{10}	6.112	0.006
f-SFX-CF_3	14.404	2.647×10^{13}	6.835×10^{9}	3.540	0.001
f-SFX-SCF_3	21.964	2.514×10^{13}	2.904×10^{10}	7.817	0.009
f-SFX-$CH_2C(O)SCF_3$	20.530	2.306×10^{13}	9.343×10^{9}	6.264	0.002

Table 9. Photovoltaic parameters for PSCs with SnO_2 ETM and devised HTMs.

HTM	Voc (V)	FF
f-SFX-$CH_2C(O)OH$	1.885	0.929
f-SFX-H	1.890	0.929
f-SFX-SH	1.892	0.929
f-SFX-OH	1.894	0.929
f-SFX-OCH_3	1.893	0.929
f-SFX-$CH_2C(O)OCH_3$	1.883	0.929
f-SFX-CH_3	1.858	0.928
f-SFX-SCH_3	1.891	0.929
f-SFX-$CH_2C(O)SCH_3$	1.887	0.929
f-SFX-$CH_2C(O)SH$	1.894	0.929
f-SFX-OCF_3	1.897	0.929
f-SFX-$CH_2C(O)OCF_3$	1.895	0.929
f-SFX-CF_3	1.898	0.929
f-SFX-SCF_3	1.897	0.929
f-SFX-$CH_2C(O)SCF_3$	1.898	0.929

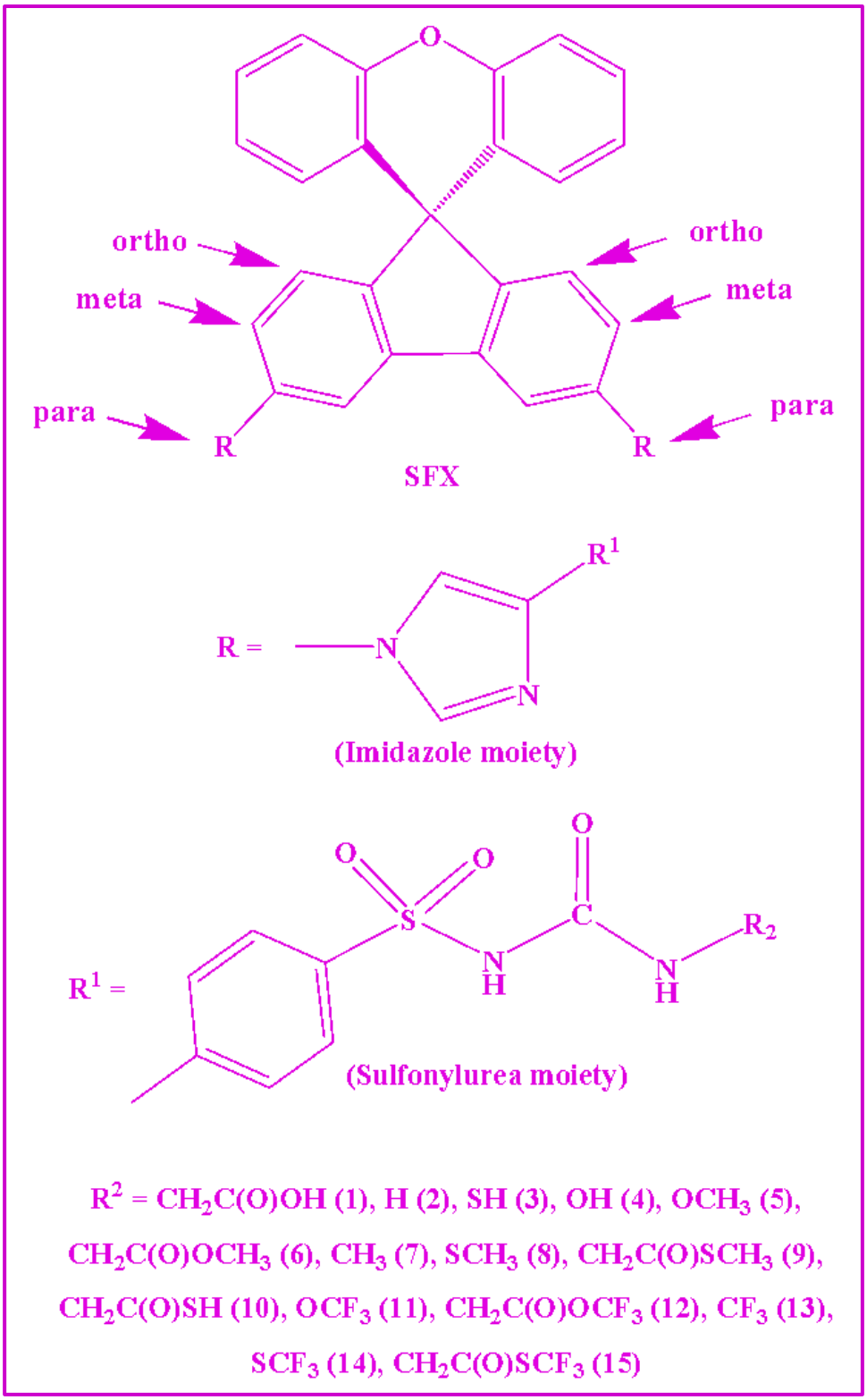

Fig. 1. Chemical structures of the designed HTMs based on the SFX skeleton containing various substituents attached to the imidazole-sulfonylurea moiety.

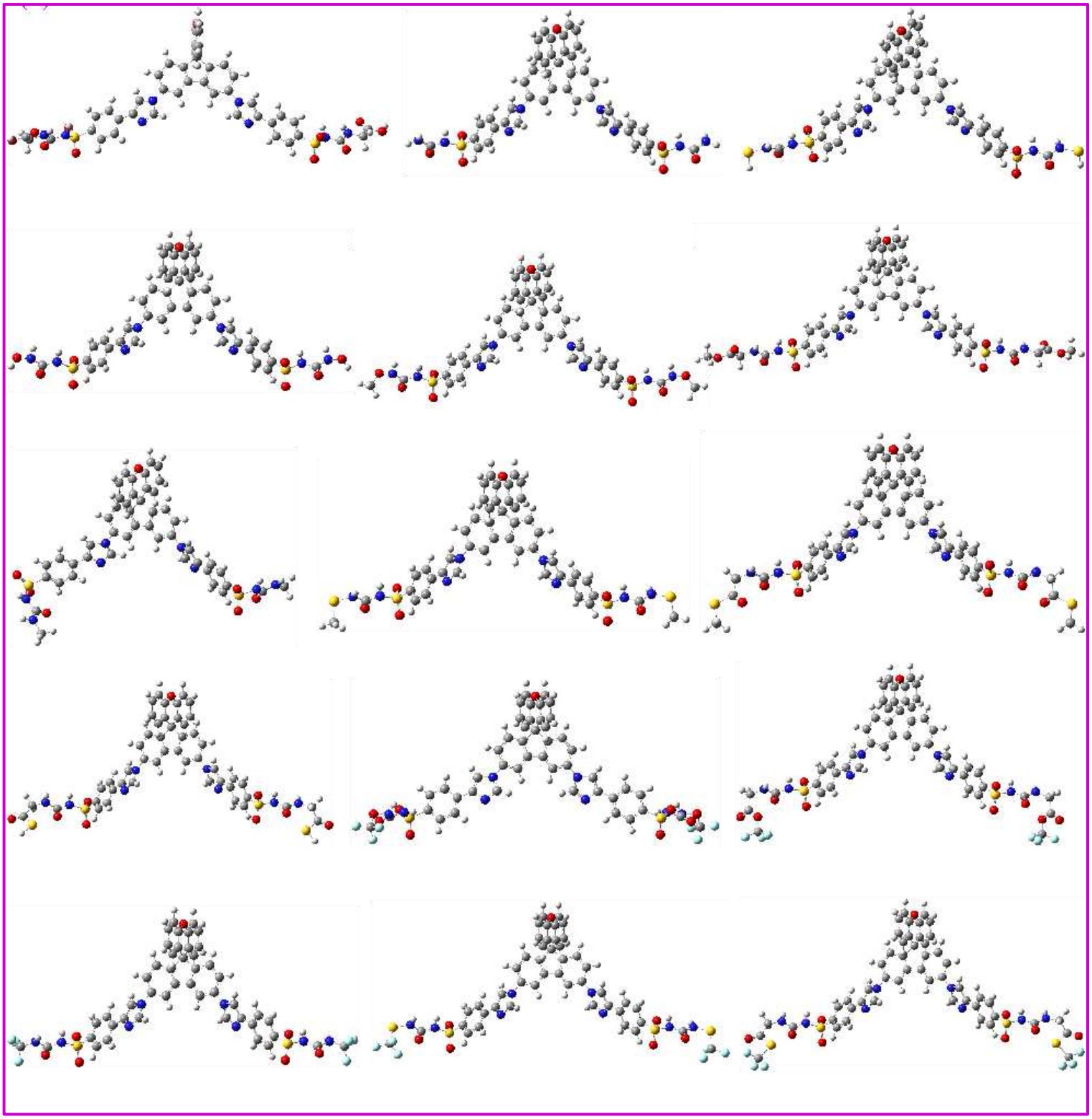

Fig. 2. The most stable structures of f-SFX-based HTM samples.

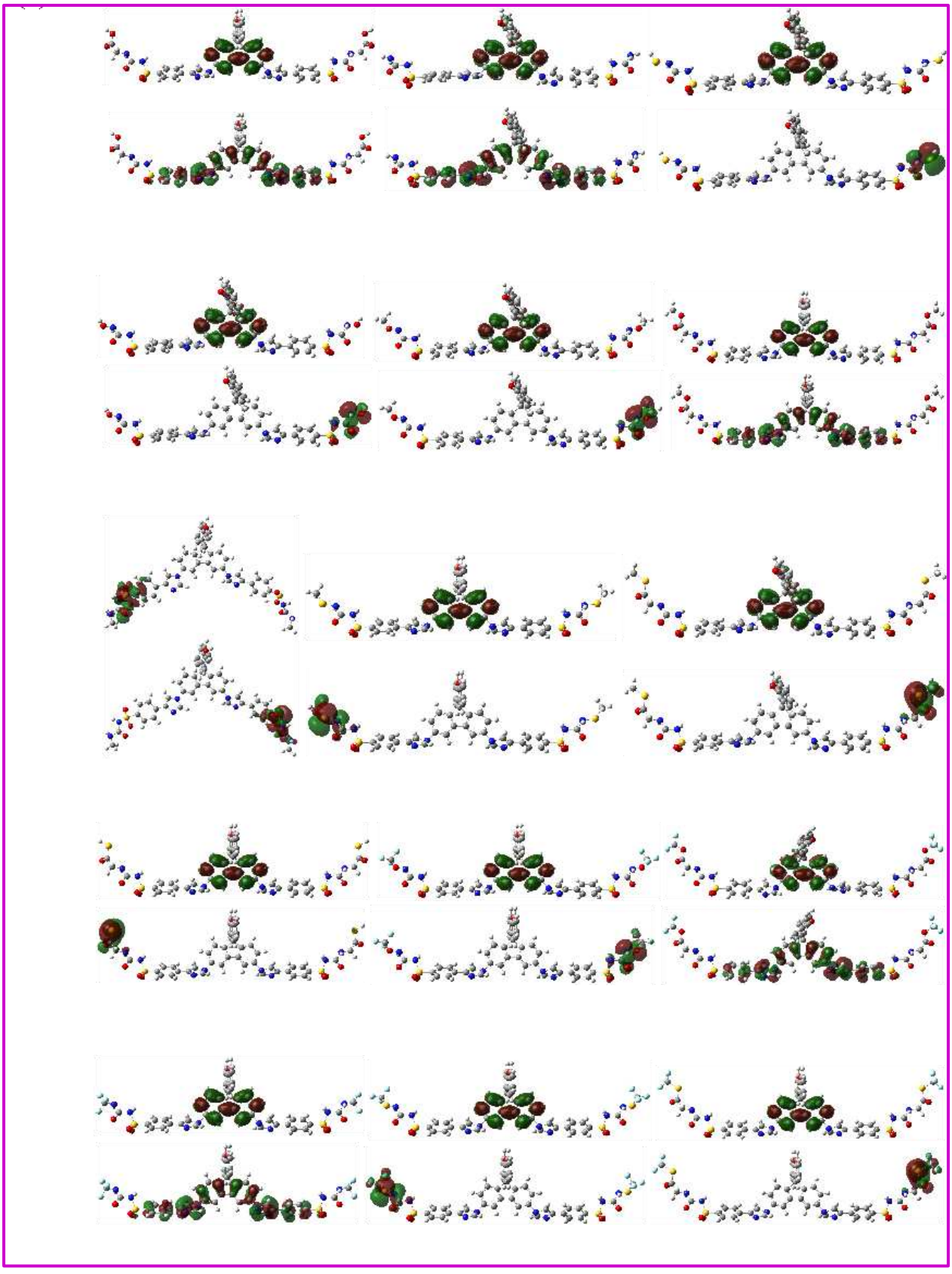

Fig. 3. FMOs of devised f-SFX-based HTMs.

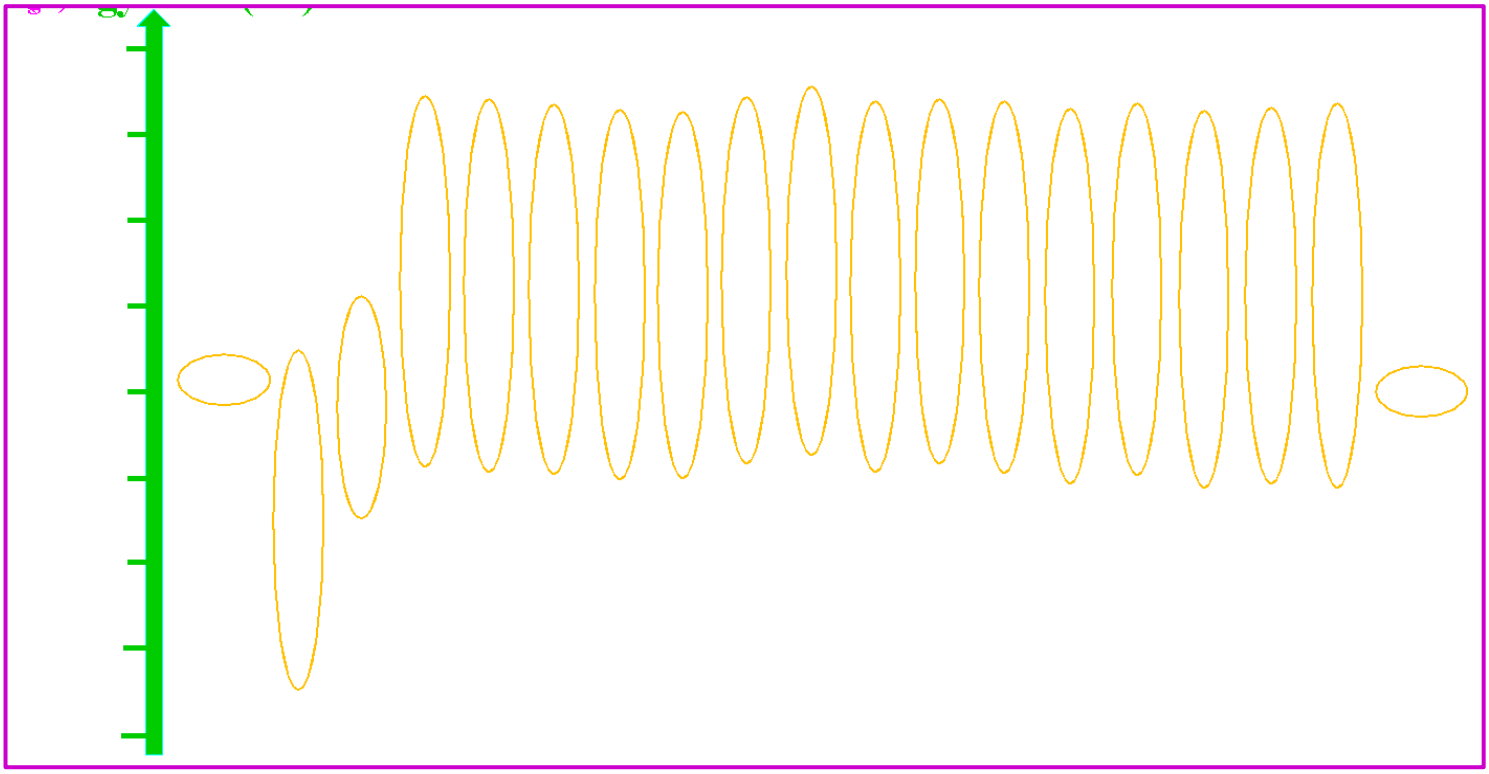

Fig. 4. Band energies of FTO, SnO_2 ETM, $CsPbCl_3$ perovskite, f-SFX-based HTMs, and Ag electrode.

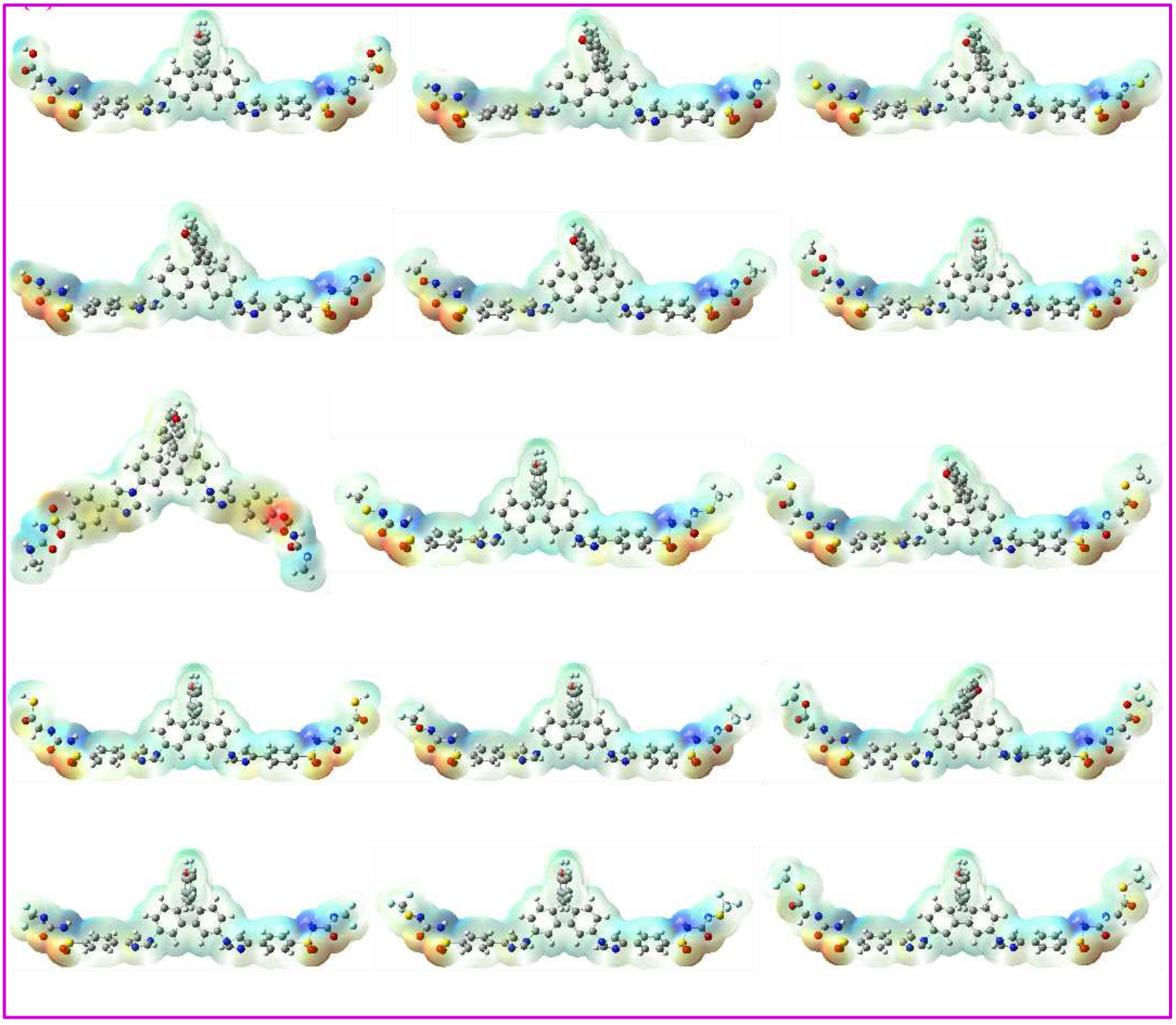

Fig. 5. Electrostatic surface potentials of devised f-SFX-based HTMs.

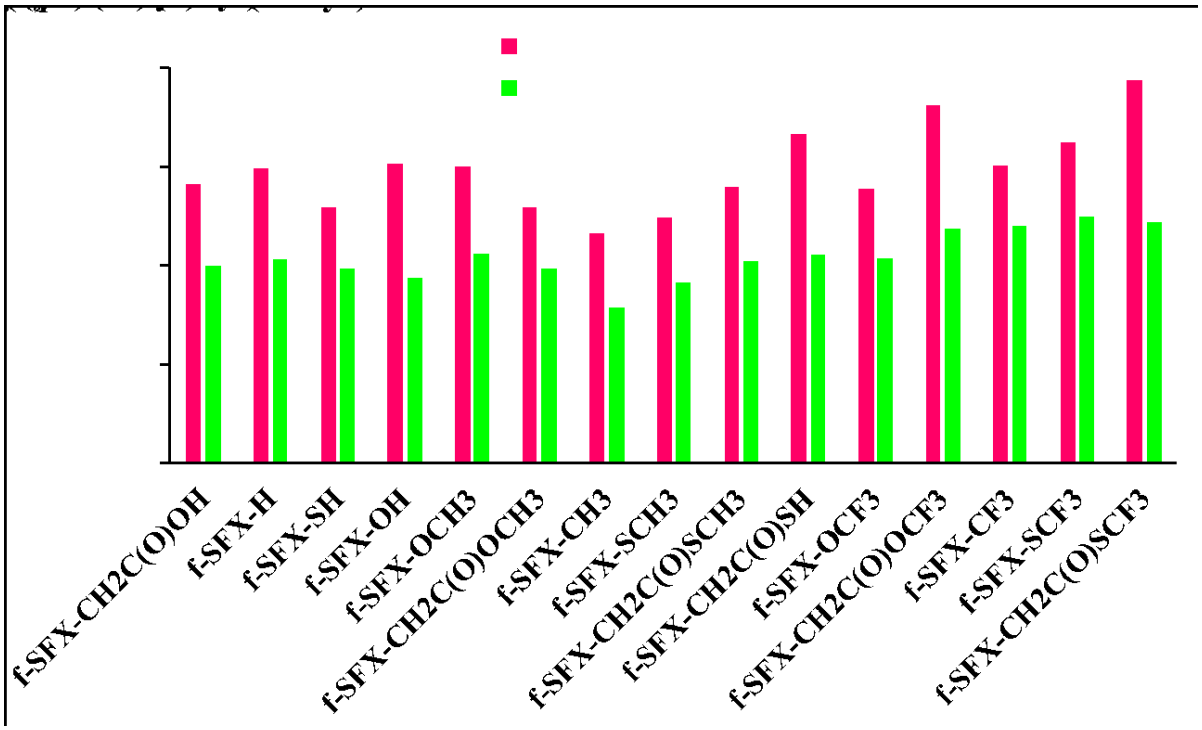
f-SFX-CH2C(O)OH
f-SFX-H
f-SFX-SH
f-SFX-OH
f-SFX-OCH3
f-SFX-CH2C(O)OCH3
f-SFX-CH3
f-SFX-SCH3
f-SFX-CH2C(O)SCH3
f-SFX-CH2C(O)SH
f-SFX-OCF3
f-SFX-CH2C(O)OCF3
f-SFX-CF3
f-SFX-SCF3
f-SFX-CH2C(O)SCF3

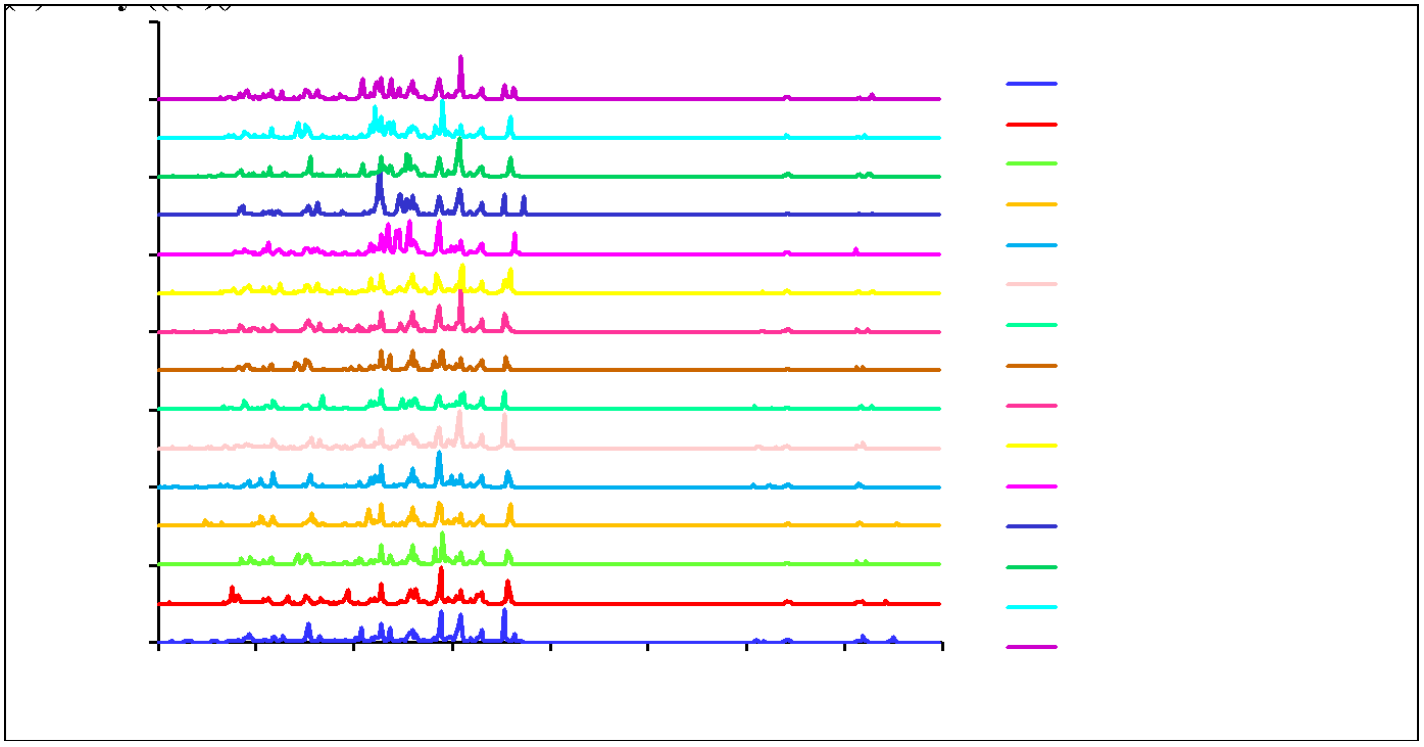

Fig. 6. (a) Changes of dipole moments of all f-SFX-based HTMs in both gas phase and dichloromethane solution. (b) Infrared spectra of HTMs within CH_2Cl_2.

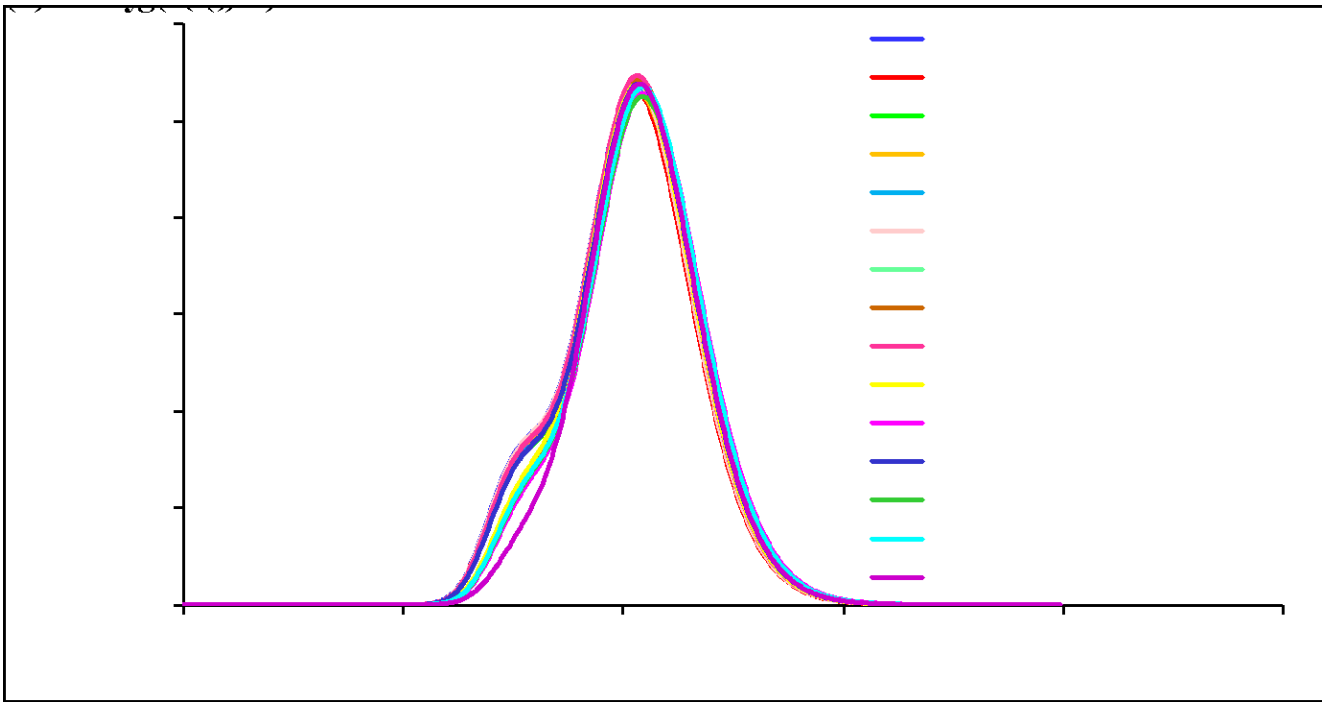

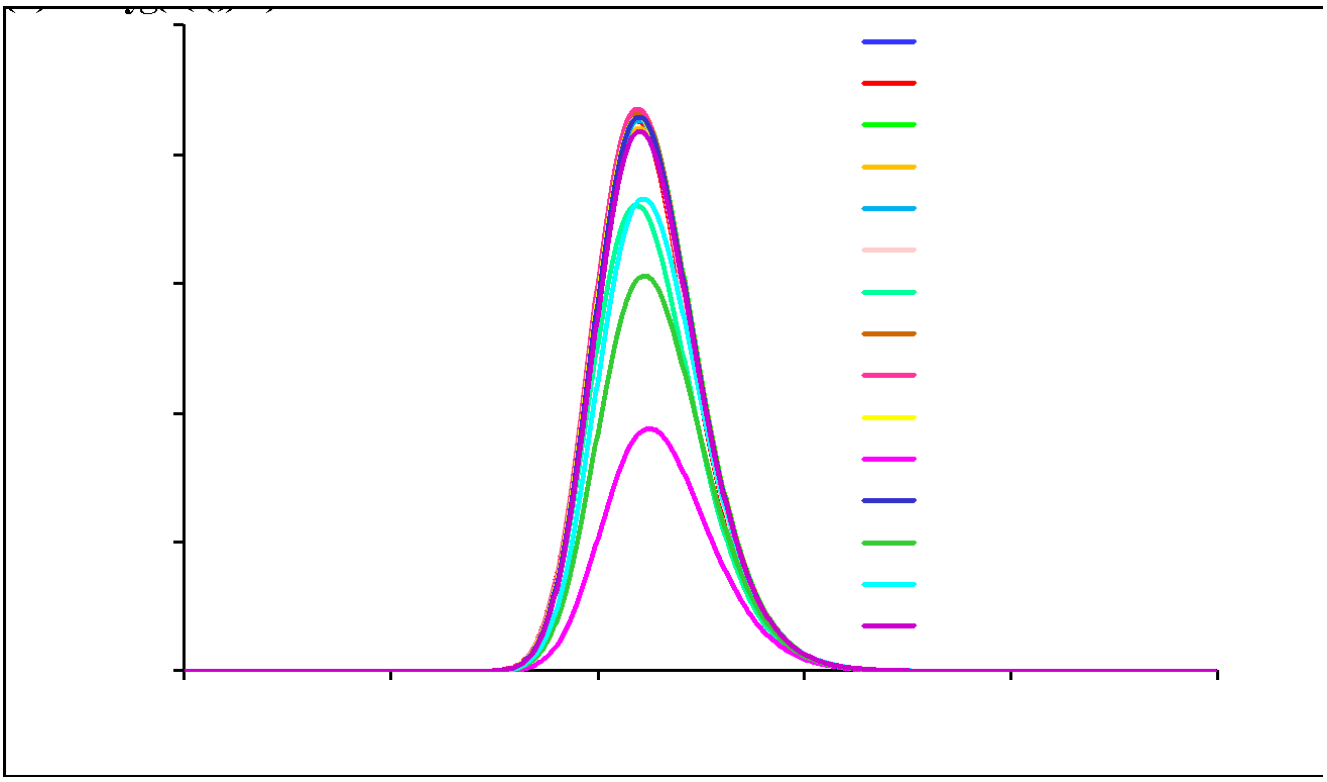

Fig. 7. (a) UV-Vis absorption and (b) PL emission spectra of f-SFX-based HTM samples within CH_2Cl_2.

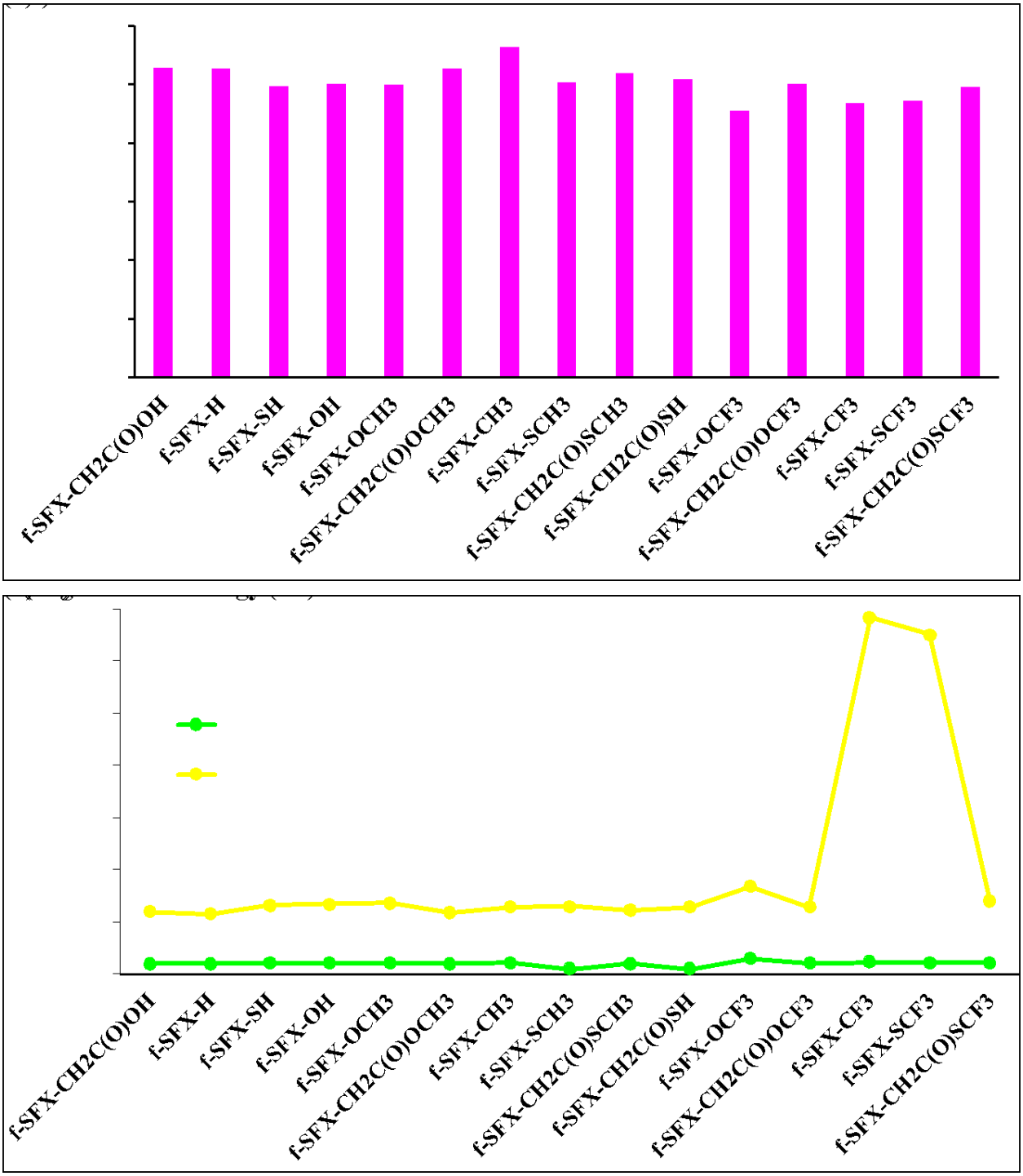

Fig. 8. Variations of (a) E_b and (b) λ_h, λ_e values of the f-SFX-based HTMs.

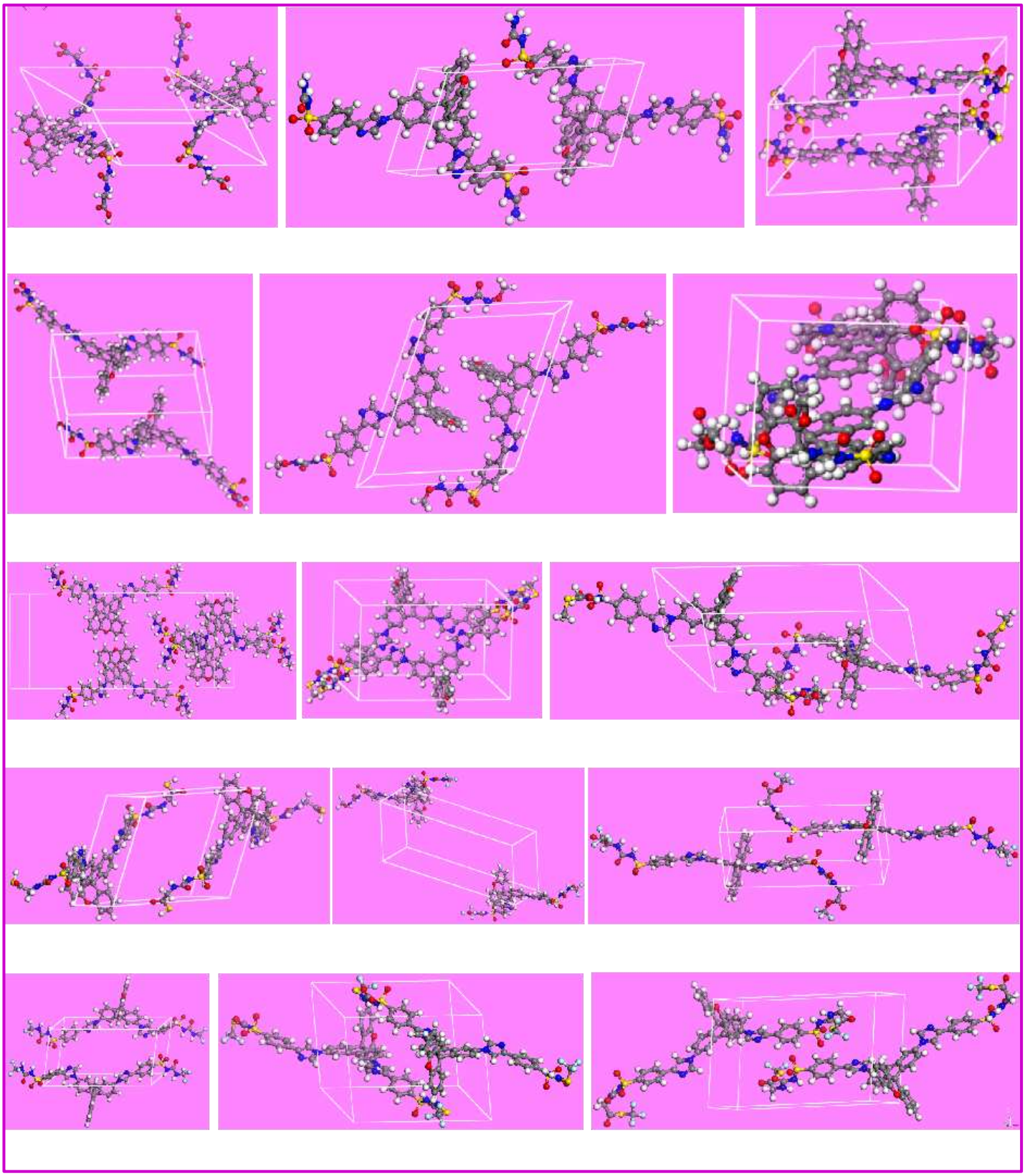

Fig. 9. The most stable unit cells of all HTMs used for calculation of hole mobility values.

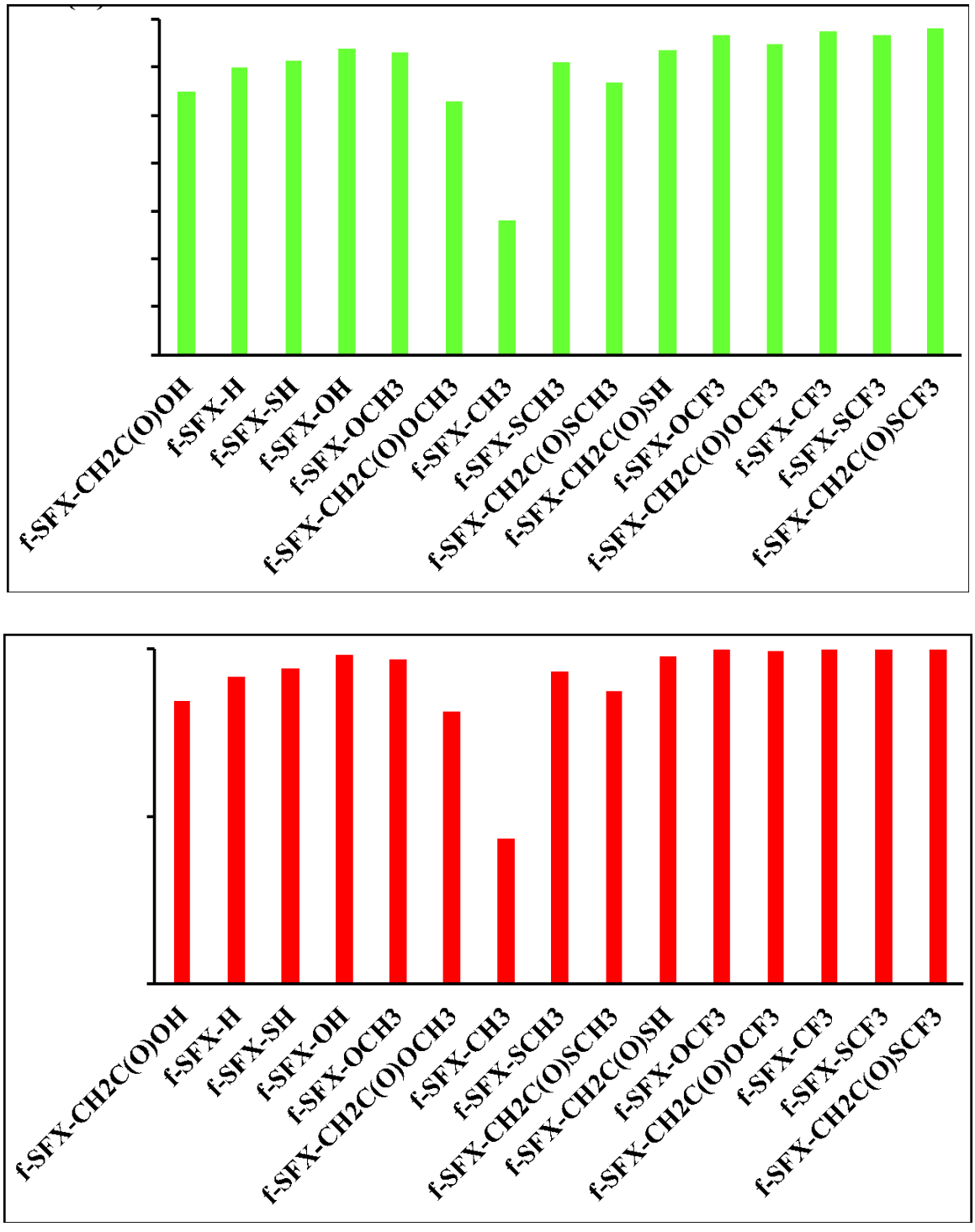

Fig. 10. V_{OC} and FF variations of f-SFX-based HTMs within CH_2Cl_2.